

Dynamics of Summer Monsoon Current around Sri Lanka

Subham Rath¹, P. N. Vinaychandran¹, J. P. McCreary², and A. Behara¹

¹Centre for Atmospheric and Oceanic Sciences, Indian Institute of Science, Bangalore, India

²International Pacific Research Center, University of Hawaii, Honolulu, Hawaii

April 21, 2022

Abstract

From June–September, the summer monsoon current (SMC) flows eastward south of Sri Lanka and turns northeastward to enter into the Bay of Bengal (BoB). The SMC is crucial for understanding exchanges between Arabian sea (AS) and BoB. The SMC shows high speeds around Sri Lanka, the reasons for which are unknown. Processes involved in the interaction of westward propagating eddies with the SMC, the meandering of the current and its ultimate termination in southeast BoB are also not well understood. In this paper, we investigate the processes that determine the evolution, intensification, and meandering of the SMC using an Indian-Ocean general circulation model (MOM4p1) and the role of local and remote forcing in modulating the dynamics of SMC. The model simulation, when compared with OSCAR data, shows good agreement. The mean seasonal circulation (June–September) shows a northeastward bending of SMC, its meandering and southeastward flow. Climatology fails to represent meandering properly. Therefore, the year 2009, arbitrary but when a strong anticyclonic bend in the SMC was observed, has been chosen for the analysis.

An eddy-kinetic-energy (EKE) budget analysis shows the region to be a zone of significant eddy activity. Both barotropic and baroclinic instability generate eddies. Based on the EKE analysis, we classify the evolution of SMC into stages of onset, intensification, anticyclonic bend, anticyclonic vortices formation, and meandering. Eddy-potential-vorticity fluxes and eddy enstrophy decay further reveal when, where, and how the eddies tend to drive the mean flow. Rossby waves and westward propagating eddies arriving from the east energise the SMC in June and induce an acceleration tendency on the mean flow through upgradient eddy potential vorticity flux.

The local winds increase the mean surface kinetic energy of the SMC and raises the isopycnals, the latter building up large amount of available potential energy (APE), and thus contribute significantly in driving the mean SMC. Baroclinic instability that takes place in late July and early August associated with the release of APE flattens the isopycnals and thus weakens the SMC. Consequently, the SMC meanders in course of time and flows into southeast BoB

1 Introduction

The Indian Ocean (IO) monsoon currents flow south of Sri Lanka and north of the equator, flowing eastward during the summer (Summer Monsoon Current; SMC) and westward during the winter (Winter Monsoon Current; WMC) [Schott and McCreary, 2001; Shankar et al., 2002]. The SMC Summer monsoon current (SMC) plays a particularly important role in the transfer of relatively salty water from the Arabian Sea (AS) to the Bay of Bengal (BoB) (Murty et al. 1992, Vinayachandran et al. 1999, Jensen 2001, Vinayachandran et al. 2013, Jensen et al. 2016).

1.1 Background

Figure 1 illustrates the SMC, providing bimonthly plots of the circulation climatology from Ocean Surface Current Analysis Real-time (OSCAR). The SMC intensifies during May, attains speeds that are high in comparison to other parts of the IO, and develops a north-eastward turn into the BoB. There are cyclonic and anticyclonic circulations just west and east of the strong current, respectively. These patterns remain during July and August, and diminish in September. They appear every year, albeit with some variations in location and timing.

By compiling the datasets obtained from satellite tracked drifting buoys, Molinari et al. (1990) observed flows along 10°N in AS and in other parts west and north of equator representing a strong eastward orientation and the flow was thus termed as the SMC. Hastenrath and Greischar (1991) described SMC as primarily wind driven. The first in situ measurements in the region using current meter moorings, found the SMC to be particularly shallow (Schott et al., 1994). Using satellite-tracked drifting buoys, Shenoi et al. (1999) reported that the SMC branched around 87°E , with one branch entering the BoB and the other continuing eastward. Expendable bathythermograph (XBT) observations collected in between Sri Lanka, Malaca Strait, altimeter data and OGCM results, showed the current to bend around Sri Lanka and flow into BoB (Vinayachandran et al., 1999).

Significant eddy activity has been reported in the region during the summer monsoon, from both drifting-buoy data (Shenoi et al., 1999) and 17 years of altimetry data (Chen et al., 2012). Large barotropic and baroclinic conversions of energy are associated with regions of high eddy energy, suggesting the importance of instabilities in their generation (Cheng et al., 2013). The first mention of intensification of SMC and its probable cause was shown in their paper which held the conversion of eddy to mean kinetic energy in June to be responsible for accelerating the SMC.

Recently, an international collaboration carried out extensive measurements to investigate monsoon-current dynamics south of Sri Lanka (Lee et al., 2016). Observations from satellite remote sensing, gliders, moorings, drifters, and echo sounders were combined to present a more comprehensive view of the circulation. After crossing the southern tip of Sri Lanka, the SMC flows around the perimeter of a distinct region of shallow thermocline, the Sri Lanka dome (SLD; Vinayachandran and Yamagata, 1998). Lee et al. (2016) also noted strong surface northward geostrophic flow along 8°N in between 83°E and 84°E .

A number of modelling studies have investigated SMC dynamics.

In companion papers, Shankar et al. (1996) and McCreary et al. (1996) found a southward flow of East Indian Coastal Current (EICC), east of Sri Lanka during the summer, surprising since the current flows *against* the southerly alongshore winds. They determined that the southward flow occurs due to local forcing by a region of strong Ekman suction just east of Sri Lanka.

McCreary et al. (1993) and Vinayachandran and Yamagata (1998) showed that the northward turning is influenced (enhanced) by the arrival of a Rossby wave associated with northward flow from the eastern boundary. Vinayachandran and Yamagata (1998) noted that both Ekman pumping and Rossby-wave arrival determined the life cycle of SLD. A large anticyclonic vortex was found to exist south of Sri Lanka along with an anticyclonic eddy east of SLD; the anticyclonic vortex was formed as a result of barotropic instability. Further, it was found that the arrival of a second Rossby-wave signal (associated with southwestward flow) terminated the northward turning.

Recently a study by Cheng et al. (2017) on the intraseasonal to semiannual variability of SSH in southern BoB revealed strong 30-60 day SSH variability east of Sri Lanka. The SSH variability east of Sri Lanka was primarily as a result of non-linear Rossby waves from the east. Further they showed that variability at periods greater than 60 days nonlinearly transferred energy to the 30-60-day band.

1.2 Present research

In this paper, we continue the effort to understand SMC dynamics. Specifically, we seek to understand the processes that cause the unusually high SMC speeds, that are involved in the interaction between the SMC and eddies, the meandering of the current, and its ultimate termination in southeastern BoB. The relative importance of winds and westward propagating eddies in modulating the mean flow in its various stages is also investigated.

To address these goals, we analyze a solution to an ocean general circulation model (OGCM) that represents the region's circulation realistically.

1.2.1 Eddy analyses

Eddy-kinetic-energy budget and Transformed Eulerian Mean framework have been used to identify regions of eddy-mean flow interactions.

1.2.2 Impact of winds

To quantify the impacts of local winds over the region, mean wind power integrated over region of interest is calculated and compared with volume integrated mean kinetic energy of SMC above the mixed layer depth. The two quantities are related to each other by mean kinetic energy equation (section 3). The geostrophic wind power which is utilised in raising the isopycnals is also integrated over the region and compared to the integrated APE.

The mean current circulation (June– September) from 2004–2009 (Fig. 2) shows the expected north eastward bending of SMC as discussed in Vinayachandran and Yamagata (1998). In addition to the already known feature, SMC was observed to meander and feed into southeast BoB in all the six years. Climatological map fails to properly capture this meandering feature of the current. There is also an inter-annual path variability in the meandering nature of the SMC. In this context, the choice of the year 2009 is arbitrary though it is primarily motivated by the study of Vinayachandran et al. (2013) which showed a sharp anticyclonic bend of the current. However, the basic mechanisms responsible for this underlying meandering feature should hold good for other years too and as such the study can be extended for other years as well .

1.2.3 Key results

- The background flow of SMC changes considerably during June – September. Looking at seasonal mean picture may not reveal the additional intricacies involved in the background SMC dynamics that varies even over a 30–day period. Daily snapshots of the SMC along with the eddy energetic conversions helped to classify the evolution of SMC in five stages, some of which have already been identified by the previous work discussed. Close inspection of 5-day OSCAR simulation of each year (2004–2009) shows the existence of the stages in all these years. So these stages prove to be general and the details of these stages complement the earlier works.
- The fact that conversion of eddy to mean kinetic energy being primarily responsible for intensification of SMC is only partially true. Our work, with the help of energy budget and TEM approach shows that the effect of eddies in intensifying the SMC is localized to a small region. The intensification of SMC is mainly dominated by the strengthening of SWM winds in the region during June–July.
- In early July, an anticyclonic bend of the SMC is noticed. No significant eddy activity is noticed during this time yet a part of SMC turns clockwise. Our study, shows that this turning is due to the ageostrophic components of the current as a result of the local winds.
- Mention of baroclinic instability as a precursor of eddy generation in the region has been talked about in earlier studies. But what effect does it have on the SMC dynamics? The baroclinic instability as a result of fluctuating geostrophic wind power is responsible for weakening of SMC and its meandering causing the current to feed into south-east BoB– a feature that is not clearly seen in the climatological maps and yet is noticed in almost individual years discussed above. The meandering of SMC is further enhanced as it meets another westward moving eddy at 8 °N. The eddy pushes against the weakened SMC and enhances the meandering. As a result of further energy exchanges, the current gradually disappears in mid September.
- The meandering feature of SMC and the processes responsible are new additions to the research. It also provides new insights into the termination of SMC.

The paper is organized as follows: Section 2 discusses model details and compares model output with observations, Section 3 is based on eddy kinetic-energy-budget analysis. Section 4 presents evolution of SMC and discusses its various stages with the help of energetics, TEM approach. Also it attempts to investigate the role of the local winds in these various stages. Section 5 provides a summary of our findings.

2 Model and solution

2.1 Model overview

The OGCM used in our study is the Modular Ocean Model (MOM), a numerical ocean model based on hydrostatic primitive equations. The model configuration, sources of forcings as well as the boundary conditions used in this study are same as in Das et al. (2015), so only a brief overview is given below.

The model domain encloses the tropical IO, extending from 30°S to 30°N and from 30–120°E. Its horizontal resolution is 0.25° in both latitude and longitude. The vertical grid has a variable resolution in the vertical with maximum of 58 levels, 44 of which are in the top 200 m with a 1-m resolution in the top 18 m. Bottom topography is based on a modified ETOPO5 bathymetry (Sindhu et al., 2007). Continental boundaries within the domain are treated as solid walls, sponge layers are applied where a boundary lies within the open ocean along the southern and portions of the eastern boundaries (Kurian and Vinayachandran, 2007). Vertical mixing follows K-profile parametrization (KPP) scheme (Large et al., 1994) while the horizontal mixing follows Chassignet and Garraffo (2001). Vertical diffusivity along with viscosity are calculated based on dissipation mechanisms associated with internal wave breaking (Simmons et al., 2004) and bottom drag experienced by barotropic tides (Lee et al., 2006). The model equation of state refers to Jackett et al. (2006).

The model is spun up for 10 years using climatological forcing, which is then switched to daily varying interannual forcing (see Vinayachandran et al. (2012) for details).

Figure 3 compares observed and modelled, surface currents during June, July, and August of 2009. Large-scale features of the circulation are represented very well in the solution, except that current speeds are underestimated. In addition, smaller-scale features, such as anticyclonic eddies during July and August, more prominent in the observations. For example, during July and August OSCAR shows a continuous meandering SMC, whereas in the solution an anticyclonic vortex is found together with the SMC as it enters the BoB. During August, two recirculation vortices are present to the right of the SMC in model. The northern recirculation vortex in the model is not prominent in the observations.

2.1.1 Background state

Let q be a model variable. Then, a key aspect of our analyses is the separation of q into mean (or slowly varying) \bar{q} and time-varying q' parts ($q = \bar{q} + q'$). Ideally, the mean (background) state should be free of high-frequency disturbances, that is, free from the influence of any

eddies. We define \bar{q} to be the model fields during 2009 smoothed by a 120-day, LSL lowpass filter, and q' to be the fields obtained using a 120-day highpass filter. We tried several cutoff periods, finding 120 days to be optimal: it is well above the residence period of mesoscale eddies in the region, and at the same time retains the large-scale seasonal variability. The background state is same for both eddy energy budget and TEM analysis. We note that a horizontal mean of the 120-day (lowpass) background state has been considered as a *reference density* state by Huang (2005).

3 Eddy activity

3.1 Mean and eddy kinetic energy

3.1.1 Equations

To investigate the eddy-mean flow interactions that impact the SMC, we divide the kinetic-energy equation for our model into mean (MKE) and eddy (EKE) parts. Following (Masina et al., 1999) and using indicial notation, MKE is defined by

$$K = \rho_0 \frac{\bar{u}_i^2}{2} \equiv \rho_0 \left(\frac{\bar{u}^2 + \bar{v}^2}{2} \right), \quad (1)$$

and determined by the prognostic equation

$$\underbrace{\frac{\partial}{\partial t} K}_A + \underbrace{\rho_0 u_j \frac{\partial}{\partial x_j} \frac{\bar{u}_i^2}{2}}_B = - \underbrace{\frac{\partial}{\partial x_i} \overline{P u_i}}_C - \underbrace{\rho_0 \bar{u}_i \frac{\partial \overline{u'_i u'_j}}{\partial x_j}}_D \underbrace{- g \bar{\rho} \bar{w}}_E + \underbrace{\bar{u}_i \cdot \bar{\mathcal{D}}}_F + \underbrace{\bar{u}_i \cdot \bar{\mathcal{F}}}_G. \quad (2)$$

A – MKE tendency

B – Advection of MKE

C – Pressure divergence flux

D – Eddy momentum flux convergence

E – Conversion mean potential energy (MPE) to MKE

F – Dissipation

G – MKE change due to external forcing

Similarly, EKE is defined by

$$K' = \rho_0 \frac{u_i'^2}{2} \equiv \rho_0 \left(\frac{u'^2 + v'^2}{2} \right), \quad (3)$$

and determined by the prognostic equation

$$\underbrace{\frac{\partial}{\partial t} K'}_{A'} + \underbrace{\rho_0 (\overline{u_j} + u'_j) \frac{\partial}{\partial x_j} \frac{u_i'^2}{2}}_{B'} = - \underbrace{\frac{\partial}{\partial x_i} (P' u'_i)}_{C'} - \underbrace{\rho_0 u'_i u'_j \frac{\partial \overline{u_i}}{\partial x_j}}_{D'} - \underbrace{g \rho' w'}_{E'} + \underbrace{u'_i \cdot \mathcal{D}'}_{F'} + \underbrace{u'_i \cdot \mathcal{F}'}_{G'}. \quad (4)$$

A' – EKE tendency

B' – Advection of EKE

C' – Eddy pressure divergence flux

D' – Deformation work due to mean flow

E' – Baroclinic energy conversion

F' – Eddy dissipation

G' – EKE change due to external forcing

3.1.2 EKE structure

Figures 4a and 4b show the time mean vertically integrated (top 100 m) map of eddy kinetic energy and its depth-longitude section at 6.5°N respectively. These values are consistent with the findings of Chen et al. (2012). Maximum eddy kinetic energy is noticed in between 83–85°E in the form of two distinct high EKE cores extending to 120 m depth. Figures 4c and 4d show the surface averaged (top 30m) time mean velocity maps and depth longitude section of velocities at 6.5°N respectively. High speeds of SMC are observed in between 83–85°E and extends upto a depth of 120m consistent with the shallow nature of SMC.

3.1.3 Time series

Figure 5 shows time series of mean kinetic energy (MKE) and eddy kinetic energy (EKE) volume integrated between 82–86°E, 5–8°N, 0–100 m. The MKE is about four times larger in magnitude as compared to EKE (Fig. 5a). This difference shows eddies only have a secondary contribution in driving the mean flow, which implies that the mean flow is largely wind driven when integrated over a larger domain. However, the effect of eddies in driving the mean flow become more significant when integrated over a smaller domain (84–85°E and 5–7°N) as the peak MKE is twice the peak EKE over the domain (Fig. 5b). Thus fractional transfer of EKE to MKE is unlikely to bring in significant changes in SMC speed throughout the domain but the effects at smaller scales are prominent as discussed later.

3.2 Instabilities

3.2.1 Instability criteria

Instabilities are associated with energy conversions. Realistic scenarios consists of both horizontal and vertical variations of energy conversions, thus leaving room for both barotropic and baroclinic instabilities (mixed instability) to commence.

3.2.2 Barotropic and baroclinic conversion terms

Barotropic instability converts MKE to EKE, and is represented by term D' of (4), which when expanded has the form

$$-\rho_0 u'_i u'_j \frac{\partial \bar{u}_i}{\partial x_j} = -\rho_0 \left(u'v' \frac{\partial \bar{u}}{\partial y} + v'v' \frac{\partial \bar{v}}{\partial y} + u'u' \frac{\partial \bar{u}}{\partial x} + u'v' \frac{\partial \bar{v}}{\partial x} \right). \quad (5)$$

Because the SMC has both zonal and meridional, velocity components, we found that the terms in (5) are of the same magnitude and hence all are retained in our analyses. Baroclinic instability converts available potential energy into EKE. It is represented by the term E' ($-g\rho'w'$) of (4). For both instability processes, positive values of terms imply conversion from energy of the background state to EKE.

3.2.3 Horizontal and vertical structure

Figure 6a, 6c shows time mean vertically integrated (100 m) maps of barotropic and baroclinic energy conversions respectively and Figure 6b, 6d represents the respective depth longitude sections of the energy conversions at 6.5°N. Barotropic energy involving both mean-eddy and eddy-mean conversions exist in between (83°E–85°E) and (5°N–7°N). Eddies are found to extract energy out of the mean flow west of 84°E through barotropic instability and transfer energy to the mean flow east of 84°E. Significant baroclinic energy conversions are also found (Fig. 6c, 6d) indicating that SMC is characterised by a mixed instability problem. Depth longitude section along 6.5°N reveals barotropic energy conversions from mean to eddy, extending to 100 m while the baroclinic energy conversion is maximum in between (60–80) m centered around 84°E.

3.3 Intraseasonal Rossby waves and eddies

Fig. 7 (top panel) is a Hovmöller diagram of high-passed meridional velocities. Westward-propagating signals with speeds of about 15.5 cm/s start at 90°E and propagate across the basin. In particular, a signal associated with northward flow is at 90°E in May and reaches 84°E by mid-June. It is followed by a signal with southward flow that arrives near 84°E about mid-July. Note that the propagation speed of the latter signal decelerates to the west (the band tilts more sharply), likely due to interaction with the SMC.

Dispersion diagram from high pass meridional velocity components (Fig. 7) shows a probable Rossby wave structure with a 40–50 day signal corresponding closely to baroclinic mode 2.

Consistent with the findings of Vinayachandran and Yamagata (1998), south and east of Sri Lanka is characterised by the interaction of Rossby waves and other probable eddies with SMC. Rossby wave phase speed calculated from the dispersion diagram is approximately 17 cm/s consistent with the Hovmöller diagram.

4 Evolution of SMC

The background flow (120-day lowpass component in our case) varies greatly during the summer monsoon. Thus processes that are significant at different phases of SMC as it evolves are presented in this section. Further, the cause of meandering of the current, will also be presented. Evolution of SMC is shown along with the dominant processes involved, for selected days of the summer monsoon of year 2009 in Figures 8–14. 5-day running average of all the quantities have been carried out to smoothen out rapid fluctuations. Evolution of SMC and the associated processes between upper layer currents, their high pass and low pass frequency components and analysis of energetics are shown. The lowpass current has a zonal orientation east of Sri Lanka at the onset of summer monsoon in late May. It gradually develops a northeastward turn in mid-June and is associated with an anticyclonic vortex in July. The current gradually meanders in August and feeds into the southeast Bay of Bengal (BoB). The evolution of SMC as viewed from energetics perspective unfolds some important features.

4.1 Onset

Onset of summer monsoon in 2009 was in late May (Das et al., 2015). With the onset, the winds become south-westerly and gain strength. Circulation around Sri Lanka during this time comprised of three different current systems – (1) a zonal flow east of Sri Lanka, (2) a southeastward current south of Sri Lanka and (3) a downwelling eddy (positive SLA) centered around 87°E , 3°N (Fig. 8a). With the advent of westward propagating eddy (3), the southeastward current merges with a zonal current around 5°N . The current is blocked by the eddy and it feeds into the zonal flow east of Sri Lanka (1). As the anticyclonic eddy approaches associated with prominent eddy kinetic energy, density surfaces along 85°E develop a poleward slope with a sharp gradient in between 5°N and 7°N (Fig. 8b). The mean kinetic energy around this time starts increasing (Fig. 8c). However, no notable barotropic or baroclinic energy conversions take place during this time.

4.2 Intensification

As the eddy moves further westward, the circulation system east of Sri Lanka is characterised by negative barotropic energy conversion (Fig. 9d). This implies wave induced accelerations to the developing SMC that is reflected in the intensification of surface currents restricted to a particular region (Fig. 9a, 10a). The current intensifies further in June with little mean

to eddy energy conversions noticed along 83°E as the southward flowing current along east coast of Sri Lanka merges with the north-eastward SMC. The 120 day highpass filtered eddy pushes the mean flow northward. The eddies thus seem to apply an acceleration tendency on the SMC (Fig. 10a).

To understand when eddies cause SMC to intensify, we use the Transformed Eulerian Mean approach to modify the momentum and density equations. The advantage of using TEM approach is that it allows the eddy forcing to appear only in the horizontal momentum equation. We also use quasi-geostrophic (QG) approximation so that the only eddy forcing in the TEM equation reduces to eddy potential vorticity (PV) flux (see Appendix). Insights from eddy enstrophy equation helps to identify where the eddies tend to drive the mean flow.

4.2.1 Where do eddies cause this intensification?

Whether the eddies tend to drive the mean flows or lead to loss of momentum in the mean flow depends on the nature of PV fluxes relative to the mean PV gradient. For eddies to drive mean flow, eddy PV flux has to be upwards relative to the mean potential vorticity gradient (Holland and Rhines, 1980), hence also known as upgradient eddy PV flux. This can be understood in terms of the general enstrophy equation (Wilson and Williams, 2004),

$$\frac{\partial q'^2}{\partial t} + \nabla \cdot \mathbf{u} \frac{q'^2}{2} + \mathbf{u}' q' \cdot \nabla \bar{q} = -D \quad (6)$$

where \bar{q} is the mean PV, q' is the eddy PV and D represents the dissipation of eddy enstrophy, all other symbols bearing their usual meanings as discussed earlier. A positive dissipation would lead to eddy enstrophy decay. First term on the left hand side of the equation (6) represents the local rate of change of eddy enstrophy, second term gives the divergence of eddy enstrophy advection and third term however gives us the eddy enstrophy decay termed here as *eddy destruction*. $\nabla \cdot \mathbf{u} (q'^2/2)$ is termed as “enstrophy destruction” term as the latter dissipates the eddies by fluxing PV into the mean flow. Negative of $\nabla \cdot \mathbf{u} (q'^2/2)$ can be thought of as generation of eddies as it leads to local increment in eddy enstrophy in (6). For the eddies to drive mean flow there has to be a decay of eddy enstrophy in the vicinity of eddy mean flow interaction. The second term can be considered as a higher order term in the equation which helps us to identify regions of convergence and divergence of eddy enstrophy flux.

Insights from the eddy destruction (Fig. 15b) help to identify regions of upgradient eddy PV flux. Here the eddies try to drive the mean flow by accelerating the latter. Regions of high velocities in the SMC are found to be associated with upgradient eddy PV flux. Upstream the eddy PV flux is downgradient indicating regions where eddies extract momentum and energy from mean flow. The region is also characterised by positive eddy PV flux downstream and negative upstream (Fig. 15c). This implies that the eddies extract momentum and energy from the SMC upstream. The same region is also barotropically unstable as found from energy considerations (Fig. 6).

4.2.2 When do eddies cause this intensification?

Time series of eddy PV flux, $v'q'$ provides a more comprehensive view of the eddy mean flow interaction. Regions where eddies tend to drive SMC are indentified (Fig. 15b) and a location has been chosen from the region. Time series of eddy PV flux at 84°E , 6.5°N and at 50 m depth indicates a sharp positive peak in mid June (Fig. 15d). This coincides with the arrival of the Rossby waves and westward propagating eddies in the region. Thus the eddies, because of positive values of $v'q'$ (see Appendix A) can be expected to provide an acceleration tendency on the mean flow as they arrive and interact with the latter in mid-June. Throughout July, eddy PV fluxes remain relatively low at the location. Positive eddy PV fluxes are observed in late August and early September but by this time SMC already starts to weaken and disappear.

4.2.3 Local winds

However, the local winds also become very strong over the region during this time and thus can influence the mean kinetic energy significantly (Fig. 9c). The mean kinetic energy of the ocean currents are related to the mean wind power in the mean kinetic energy equation (2) as

$$\int_V \rho_0 \frac{\partial \overline{\mathbf{u}^2}}{\partial t} dV \sim \int_A \overline{\mathcal{F} \cdot \mathbf{u}} dA = \int_A \overline{\boldsymbol{\tau} \cdot \mathbf{u}} dA \quad (7)$$

τ is the wind stress. Figure 18(a) and Figure 18(b) shows the variation of mean windpower input along with mean surface kinetic energy, integrated over top 40 m within surface mixed layer. Both the quantities are integrated over $82\text{--}86^\circ\text{E}$, $5\text{--}8^\circ\text{N}$. The mean kinetic energy increases with increase in total mean wind power in June, peaks in late June following the variation of mean wind power and starts to decline from mid July. Thus the winds can be considered as the predominant driving agent in intensifying mean SMC flow.

4.3 Anticyclonic bend

At the beginning of July, part of the SMC starts taking an anticyclonic turn about 85°E , while the other part continues to flow northeastward (Fig. 11a, 11c). The mean kinetic energy is high in the region during this time (Fig. 11c) while the eddy kinetic energy is significantly low (Fig. 11e). Barotropic energy conversions are also very small (Fig. 11d). However, some amount of baroclinic energy conversions take place north of the SMC where it takes a cyclonic turn (Fig. 11f). Density surfaces within 40–100 m along 85°E is suppressed in between 5°N and 7°N with a poleward gradient resulting in the generation of available potential energy. In mid July, the anticyclonic turn of the SMC becomes more prominent associated with high mean kinetic energy but low eddy kinetic energy. Barotropic energy conversions are very low in the region, while positive baroclinic energy conversions are found along the SMC. Negative baroclinic energy conversions implying an increase in eddy available potential energy is found on either sides of the SMC. But this does not adequately explain the bending of SMC. The anticyclonic turning of the lowpass current can also be due to

the local winds in the region. The ageostrophic component of the current supports this possibility (Fig. 16). The ageostrophic currents are higher and modulate the background flow in the absence of prominent eddies over the region during the time. The baroclinic energy conversions observed can be due to the variation in the wind energy input, leading to the fluctuation of the density surfaces (discussed next).

4.4 Anticyclonic vortices

In late July (Fig. 12a), SMC has an anticyclonic vortex fully developed, centered around 84°E. In addition to the anticyclonic turning of the lowpass background current, an anticyclonic eddy associated with strong eddy kinetic energy is found in this region. Both barotropic and baroclinic energy conversions are responsible for the generation of eddies. SMC at 83°E, 6°N becomes barotropically unstable leading to conversion of mean kinetic energy to eddy kinetic energy (Fig. 12d). Baroclinic instability also take place around 7°N associated with flattening of isopycnals that weaken the flow and can cause the current to meander (Fig. 12f). Significant baroclinic energy conversions are noticed all along the outer periphery of the anticyclonic vortex.

In mid July, at around 89°E, 8°N, SMC meets another anticyclonic eddy which remains non interacting. Later in late July, due to the gradual meandering pattern of the current, the eddy around 8°N further intrudes into the SMC (Fig. 12a). This eddy was termed as an Intermediate Geostrophic (IG) eddy (Vinayachandran and Yamagata, 1998).

4.5 Meandering

Horizontal shear of the SMC reduces as a result of barotropic instability. Further, in early August (Fig. 13b), the sloping density surfaces flatten releasing large amount of Available Potential Energy (APE). Baroclinic instability associated with this flattening of density gradients and meridional buoyancy flux is the dominant mechanism leading to the growth of disturbances (Fig. 13f). The combined effect of barotropic and baroclinic instability weakens the SMC which now meanders because of baroclinic instability (Ikeda, 1981). One possible reason behind the release of APE in late July and August, can be the gradual weakening of local winds power.

4.5.1 Local wind power

The wind power is calculated as;

$$W = \iint_A \boldsymbol{\tau} \cdot \mathbf{u} dA, = \iint_A (\boldsymbol{\tau} \cdot \mathbf{u}_g + \boldsymbol{\tau} \cdot \mathbf{u}_{ag}) dA,$$

$\boldsymbol{\tau} \cdot \mathbf{u}_g$ is the geostrophic wind power while $\boldsymbol{\tau} \cdot \mathbf{u}_{ag}$ is the ageostrophic wind power. The geostrophic wind work is utilised in vertically displacing the isopycnals thereby influencing

available potential energy (APE) (Brown and Fedorov, 2010) by Ekman pumping, upwelling and downwelling. On the other hand, the ageostrophic wind work is required to maintain the Ekman spiral (Huang, 2010).

Figure 17 shows time-mean (June–September) monthly maps of total wind power (combining geostrophic and ageostrophic), baroclinic energy conversions, mean and EKE, vertically integrated over 100 m. Wind power is positive maximum in region of our interest south east of Sri Lanka. The mean and eddy kinetic energy together with baroclinic energy conversions are also found to be significantly high over this region.

4.5.2 Available potential energy

Available potential energy (APE) can be defined as difference between total potential energy and minimum total potential energy which could result from any adiabatic redistribution of mass. It vanishes if density stratification is horizontal, statically stable everywhere, positive otherwise (Huang, 2005). It can thus also be regarded as a deviation from the *rest stable stratification* state. Here in order to estimate local APE, it is calculated (Joules) as (Oort et al., 1989)

$$E_p = -\frac{g}{2} \iiint_V \frac{(\rho - \bar{\rho})^2}{\partial \bar{\rho} / \partial z} dV. \quad (8)$$

APE has been integrated over 82–86°E, 5–8°N and from the surface to 100 m.

Figure 18(c) and Figure 18(d) shows the relationship between wind power and volume integrated available potential energy. The available potential energy corresponds well with the variation in wind power. Only in the month of June, the available potential energy remains unchanged for some time inspite of increasing wind power. Arrival of downwelling Rossby waves associated with suppressed thermocline can negate the influence of wind power. In late June, APE again starts to respond to change in wind power. During this time, the local wind power probably overrides the effects of remotely forced eddies. Significant amount of APE reduction starts from mid-July and continues till August and is associated with the possibility of major baroclinic instability mechanism taking place at the depth.

In addition to the winds, remotely forced westward propagating eddies can cause the current to meander.

4.5.3 Westward propagating eddies

Earlier, the westward propagating eddy at 8°N did not interact with the SMC (Fig. 12d, 12f). The eddy starts interacting with the meandering current in this stage (Fig. 13d, 13f). One possible reason can be the weakening of SMC as a result of baroclinic instability, which now has *critical levels* (levels where exchange of energy takes place between mean flow and wave). The interaction of this eddy with SMC leads to barotropic instability at 85°E, 6°N with an immediate eddy to mean conversion adjacent to it (Fig. 13d). This renders the current barotropically unstable and merely amplifies the recirculation at 8°N and the current is thus found to meander and feed into south east BoB (Fig. 13a).

4.6 Termination

In late August and September, the continuous SMC system disappears (Fig. 14a). The anticyclonic eddy around 8°N pushing against the weakened SMC moves westward. The entire meandering pattern shifts slightly to the west and by mid-September (Fig. 14a) the SMC system disappears.

5 Summary and conclusions

Summer monsoon current (SMC) around Sri Lanka plays a crucial role in the interaction of the watermasses between the two basins on either sides of India, Arabian Sea (AS) and Bay of Bengal (BoB), and yet little is known about its dynamics. Past studies have shown that the SMC is highly energetic and eddy activity is intense in this region (Vinayachandran and Yamagata, 1998, Shenoi et al., 1999, Chen et al., 2012). The prime objective of the analysis was to understand the evolution, intensification and meandering of the SMC using an OGCM (MOM4p1) simulation. The role of remotely forced Rossby waves and eddies as well as local winds in influencing the SMC dynamics were also investigated.

The study has made several new contributions towards understanding the evolution of SMC around Sri Lanka, which involves eddy mean flow interactions and effect of local versus remote forcing on the dynamics over the region. Analysis of eddy potential vorticity fluxes, eddy enstrophy, eddy energy budgets carried out in this study have shed new insights on how the eddies drive mean flow and vice versa. The study has also helped in a better understanding of the influence of stratification in driving the mean flow and in isolating role of winds in affecting the circulation.

The evolution of SMC was classified into five stages namely onset, intensification, anticyclonic bend, anticyclonic vortices and meandering. Barotropic and baroclinic energy conversions are the dominant mechanisms to modulate the background flow of SMC during this time. The arrival of Rossby waves and westward propagating eddies into this region have resulted in high eddy momentum flux exchanges in the month of June. Using a Transformed Eulerian Mean approach and combining the net effect of momentum and buoyancy fluxes, it was shown that the eddies imparted potential vorticity flux and induced acceleration tendency on the background flow in mid June. Using quasigeostrophic approximation to understand the effect of eddies on mean flow, it was found that there were regions of upgradient eddy PV fluxes where the eddies drove the time mean flow. There were also regions upstream associated with downgradient eddy PV fluxes where the eddies extracted energy and momentum out of the mean flow.

Local winds affected both the mean flow of SMC and its course during the summer monsoon. The volume integrated mean kinetic energy was atleast twice that of eddy kinetic energy (EKE) suggesting that the circulation in this region is largely wind driven. Also the time mean maps of mean kinetic energy corresponded well with the wind power. Time series of surface average ocean kinetic energy revealed strong correspondence with the time series of area integrated total mean wind power implying the dominant influence of local winds in

driving the mean currents. The geostrophic wind power also modulated the density surfaces thereby influencing the APE except in mid June. One explanation for such behaviour can be the arrival of downwelling Rossby waves associated with suppressed thermocline and thereby trying to negate the effects of winds. The variation in wind power led to generation of eddies in the region through baroclinic energy conversions (APE to EKE).

It may be noted that the analysis presented here has certain limitations. Non linearities involved in our model can accelerate or suppress features that may arise from linearized assumptions which is a limitation of the theory. There are several issues that future studies can address in order to have a complete understanding of the dynamics of SMC. Conducting idealised experiments by segregating forcings under linearized set of equations with small perturbations may be useful. The analysis in this study has been carried out for one year. Even though this general behavior of the SMC is similar every year, there can be considerable variability from year to year. Therefore it is useful to carry out the analysis for a longer period.

Acknowledgments

This research was supported by Ministry of Human Resource Development (MHRD) funding. OSCAR data provided by NOAA-NASA (<http://dx.doi.org/10.5067/OSCAR-03D01>), QuikSCAT winds by IFREMER (<http://www.ifremer.fr/cersat/en/data/data.htm>) were used for the study. Computations were carried out on a high performance computer (HPC) system facility funded by Department of Science and Technology under Fund for Improvement of ST Infrastructure in Universities and Higher Educational Institutions (FIST) scheme at Center for Atmospheric and Oceanic Sciences (CAOS), Indian Institute of Science, Bangalore and Divecha Center for Climate Change (DCCC). The authors are thankful to GFDL for providing the MOM4p1 source code. Ferret and Matlab has been used for data analysis and graphics output.

Appendices

A TEM equations

A.0.1 Equations of motion

The horizontal momentum and buoyancy equations can be decomposed into a mean and perturbation part as shown in (1). These equations under quasigeostrophic (QG) approximation in Reynold's averaged form become

$$\frac{\partial \overline{\mathbf{u}}_g}{\partial t} + \overline{\mathbf{u}}_g \cdot \nabla \overline{\mathbf{u}}_g + f_0 \mathbf{k} \times \overline{\mathbf{u}}_{ag} + \beta y \mathbf{k} \times \overline{\mathbf{u}}_g - \frac{\nabla \overline{p}_{ag}}{\rho_0} = \mathbf{G} - \nabla \cdot \overline{\mathbf{u}'\mathbf{u}'}, \quad (9)$$

$$\nabla_h \cdot \overline{\mathbf{u}}_{ag} + \frac{\partial \overline{w}_{ag}}{\partial z} = 0, \quad (10)$$

$$\frac{\partial \bar{b}}{\partial t} + \overline{\mathbf{u}}_g \cdot \nabla \bar{b} + \overline{w}_{ag} N_0^2 = X - \nabla \cdot \overline{\mathbf{u}'b'}, \quad (11)$$

where \mathbf{u}_g represents geostrophic velocities, the overbar denotes the 120-day, low-pass-filtered background state and the primed quantities represent high-pass-filtered eddies. u_{ag} , w_{ag} are the ageostrophic components, b represents the buoyancy and G , X are forcing terms. Thus the effect of eddies on background state appear in two equations (Eqs. 9 and 11) represented by the convergence of eddy momentum fluxes, $-\nabla \cdot \overline{\mathbf{u}'\mathbf{u}'}$ and buoyancy flux, $-\nabla \cdot \overline{\mathbf{u}'b'}$.

Apart from having an acceleration tendency on background flow, the momentum flux can also drive the horizontal mean ageostrophic flow. Also, the buoyancy fluxes can drive the mean flow implying the dynamical coupling between density and momentum equations. It is not thus possible to view how the density fluxes may accelerate or decelerate the background flow. Transformed Eulerian mean (TEM) approach helps us to get rid of this problem as a result of which only the eddy forcing appears in the horizontal momentum equations. The TEM equations can be written as

$$\frac{\partial \widetilde{\mathbf{u}}_g}{\partial t} + \widetilde{\mathbf{u}}_g \cdot \nabla \widetilde{\mathbf{u}}_g + f_0 \mathbf{k} \times \widetilde{\mathbf{u}}_{ag} + \beta y \mathbf{k} \times \widetilde{\mathbf{u}}_g - \frac{\nabla \widetilde{p}_{ag}}{\rho_0} = \mathbf{G} - \underbrace{\nabla \cdot \widetilde{\mathbf{E}}}_{EF}, \quad (12)$$

$$\nabla_h \cdot \widetilde{\mathbf{u}}_{ag} + \frac{\partial \widetilde{w}_{ag}}{\partial z} = 0, \quad (13)$$

$$\frac{\partial \bar{b}}{\partial t} + \widetilde{\mathbf{u}}_g \cdot \nabla \bar{b} + \widetilde{w}_{ag} N_0^2 = X \quad (14)$$

where EF = eddy forcing. The tilde over the ageostrophic circulation terms represents the residual mean circulation. In many cases, the mean ageostrophic circulation can negate the impact of eddies. The residual mean circulation represents the net effect of the two quantities. Eddy components are given by the eddy bolus velocities,

$$\mathbf{u}^* = -\frac{\partial}{\partial z} \frac{\overline{b'\mathbf{u}'}}{N_0^2}, \quad \mathbf{w}^* = \nabla \cdot \frac{\overline{b'\mathbf{u}'}}{N_0^2}. \quad (15)$$

B Eddy potential vorticity flux

Vector \mathbf{E} in (12) represents the eddy-stress tensor (Plumb, 1986). The advantage of using the QG approximation to understand eddy-driven mean flows is that it expresses the divergence of eddy stress tensor explicitly in terms of eddy potential-vorticity flux.

$$\nabla \cdot \mathbf{E} \approx -\hat{\mathbf{k}} \times \overline{q'\mathbf{u}'}, \quad (16)$$

where

$$q'\mathbf{u}' = \nabla \cdot \begin{pmatrix} N & M - P & 0 \\ M - P & -N & 0 \\ R & S & 0 \end{pmatrix}, \quad (17)$$

$M = (\overline{v'^2} - \overline{u'^2})/2$, $N = \overline{u'v'}$, $P = (\overline{b'^2}/2) N^2$, $R = \overline{v'b'}$, and $S = (f_0/N_0^2) \overline{u'b'}$. Variables M and N are the eddy momentum flux, P is the eddy potential energy, and R and S are the meridional and zonal eddy buoyancy fluxes under the QG assumption. Although both eddy momentum and buoyancy fluxes impact the mean flow, considering their effects separately can sometimes be misleading. This problem is avoided in \mathbf{E} , which combines the influence of the two fluxes. The component of \mathbf{E} normal to the mean flow tends to accelerate or decelerate it, whereas the component parallel to the mean flow tends to turn it.

References

- Brown, J. N. and Fedorov, A. V. (2010). How much energy is transferred from the winds to the thermocline on enso time scales? *Journal of Climate*, 23(6):1563–1580.
- Chassignet, E. P. and Garraffo, Z. D. (2001). Viscosity parameterization and the gulf stream separation. Technical report, DTIC Document.
- Chen, G., Wang, D., and Hou, Y. (2012). The features and interannual variability mechanism of mesoscale eddies in the bay of bengal. *Continental Shelf Research*, 47:178–185.
- Cheng, X., McCreary, J. P., Qiu, B., Qi, Y., and Du, Y. (2017). Intraseasonal-to-semiannual variability of sea-surface height in the eastern, equatorial indian ocean and southern bay of bengal. *Journal of Geophysical Research: Oceans*.
- Cheng, X., Xie, S.-P., McCreary, J. P., Qi, Y., and Du, Y. (2013). Intraseasonal variability of sea surface height in the bay of bengal. *Journal of Geophysical Research: Oceans*, 118(2):816–830.
- Das, U., Vinayachandran, P., and Behara, A. (2015). Formation of the southern bay of bengal cold pool. *Climate Dynamics*, pages 1–15.
- Hastenrath, S. and Greischar, L. (1991). The monsoonal current regimes of the tropical indian ocean: Observed surface flow fields and their geostrophic and wind-driven components. *Journal of Geophysical Research: Oceans*, 96(C7):12619–12633.
- Holland, W. R. and Rhines, P. B. (1980). An example of eddy-induced ocean circulation. *Journal of Physical Oceanography*, 10(7):1010–1031.
- Huang, R. X. (2005). Available potential energy in the world’s oceans. *Journal of Marine Research*, 63(1):141–158.
- Huang, R. X. (2010). *Ocean circulation: wind-driven and thermohaline processes*. Cambridge University Press.
- Ikeda, M. (1981). Meanders and detached eddies of a strong eastward-flowing jet using a two-layer quasi-geostrophic model. *Journal of Physical Oceanography*, 11(4):526–540.
- Jackett, D. R., McDougall, T. J., Feistel, R., Wright, D. G., and Griffies, S. M. (2006). Algorithms for density, potential temperature, conservative temperature, and the freezing temperature of seawater. *Journal of Atmospheric and Oceanic Technology*, 23(12):1709–1728.
- Jensen, T. G. (2001). Arabian sea and bay of bengal exchange of salt and tracers in an ocean model. *Geophys. Res. Lett*, 28(20):3967–3970.

- Jensen, T. G., Wijesekera, H. W., Nyadjro, E. S., Thoppil, P. G., Shriver, J. F., Sandeep, K., and Pant, V. (2016). Modeling salinity exchanges between the equatorial indian ocean and the bay of bengal. *Oceanography*, 29(2):92–101.
- Kurian, J. and Vinayachandran, P. (2007). Mechanisms of formation of the arabian sea mini warm pool in a high-resolution ocean general circulation model. *Journal of Geophysical Research: Oceans*, 112(C5).
- Large, W. G., McWilliams, J. C., and Doney, S. C. (1994). Oceanic vertical mixing: A review and a model with a nonlocal boundary layer parameterization. *Reviews of Geophysics*, 32(4):363–403.
- Lee, C. M., Jinadasa, S., Anutaliya, A., Centurioni, L. R., Fernando, H. J., Hormann, V., Lankhorst, M., Rainville, L., Send, U., and Wijesekera, H. W. (2016). Collaborative observations of boundary currents, water mass variability, and monsoon response in the southern bay of bengal. *Oceanography*, 29(2):102–111.
- Lee, I., Liu, J. T., et al. (2006). Rectification of the heading and tilting of sediment trap arrays due to strong tidal currents in a submarine canyon. *Geophysical research letters*, 33(8).
- Masina, S., Philander, S., and Bush, A. (1999). An analysis of tropical instability waves in a numerical model of the pacific ocean: 2. generation and energetics of the waves. *Journal of Geophysical Research: Oceans*, 104(C12):29637–29661.
- McCreary, J., Han, W., Shankar, D., and Shetye, S. (1996). Dynamics of the east india coastal current: 2. numerical solutions. *Journal of Geophysical Research: Oceans*, 101(C6):13993–14010.
- Molinari, R. L., Olson, D., and Reverdin, G. (1990). Surface current distributions in the tropical indian ocean derived from compilations of surface buoy trajectories. *Journal of Geophysical Research: Oceans*, 95(C5):7217–7238.
- Murty, V., Sarma, Y., Rao, D., and Murty, C. (1992). Water characteristics, mixing and circulation in the bay of bengal during southwest monsoon. *Journal of Marine Research*, 50(2):207–228.
- Oort, A. H., Ascher, S. C., Levitus, S., and Peixóto, J. P. (1989). New estimates of the available potential energy in the world ocean. *Journal of Geophysical Research: Oceans*, 94(C3):3187–3200.
- Plumb, R. A. (1986). Three-dimensional propagation of transient quasi-geostrophic eddies and its relationship with the eddy forcing of the time-mean flow. *Journal of the atmospheric sciences*, 43(16):1657–1678.

- Schott, F., Reppin, J., Fischer, J., and Quadfasel, D. (1994). Currents and transports of the monsoon current south of sri lanka. *Journal of Geophysical Research: Oceans*, 99(C12):25127–25141.
- Schott, F. A. and McCreary, J. P. (2001). The monsoon circulation of the indian ocean. *Progress in Oceanography*, 51(1):1–123.
- Shankar, D., McCreary, J., Han, W., and Shetye, S. (1996). Dynamics of the east india coastal current: 1. analytic solutions forced by interior ekman pumping and local alongshore winds. *Journal of Geophysical Research: Oceans*, 101(C6):13975–13991.
- Shankar, D., Vinayachandran, P., and Unnikrishnan, A. (2002). The monsoon currents in the north indian ocean. *Progress in oceanography*, 52(1):63–120.
- Shenoi, S., Saji, P., and Almeida, A. (1999). Near-surface circulation and kinetic energy in the tropical indian ocean derived from lagrangian drifters. *Journal of Marine Research*, 57(6):885–907.
- Simmons, H. L., Jayne, S. R., Laurent, L. C. S., and Weaver, A. J. (2004). Tidally driven mixing in a numerical model of the ocean general circulation. *Ocean Modelling*, 6(3):245–263.
- Sindhu, B., Suresh, I., Unnikrishnan, A., Bhatkar, N., Neetu, S., and Michael, G. (2007). Improved bathymetric datasets for the shallow water regions in the indian ocean. *Journal of Earth System Science*, 116(3):261–274.
- Vinayachandran, P., Masumoto, Y., Yamagata, T., and Mikawa, T. (1999). Intrusion of the southwest monsoon current into the bay of bengal. *Journal of Geophysical Research*, 104(C5):11077–11085.
- Vinayachandran, P., Neema, C., Mathew, S., and Remya, R. (2012). Mechanisms of summer intraseasonal sea surface temperature oscillations in the bay of bengal. *Journal of Geophysical Research: Oceans*, 117(C1).
- Vinayachandran, P., Shankar, D., Vernekar, S., Sandeep, K., Amol, P., Neema, C., and Chatterjee, A. (2013). A summer monsoon pump to keep the bay of bengal salty. *Geophysical Research Letters*, 40(9):1777–1782.
- Vinayachandran, P. and Yamagata, T. (1998). Monsoon response of the sea around sri lanka: generation of thermal domes and anticyclonic vortices. *Journal of Physical Oceanography*, 28(10):1946–1960.
- Wilson, C. and Williams, R. G. (2004). Why are eddy fluxes of potential vorticity difficult to parameterize? *Journal of physical oceanography*, 34(1):142–155.

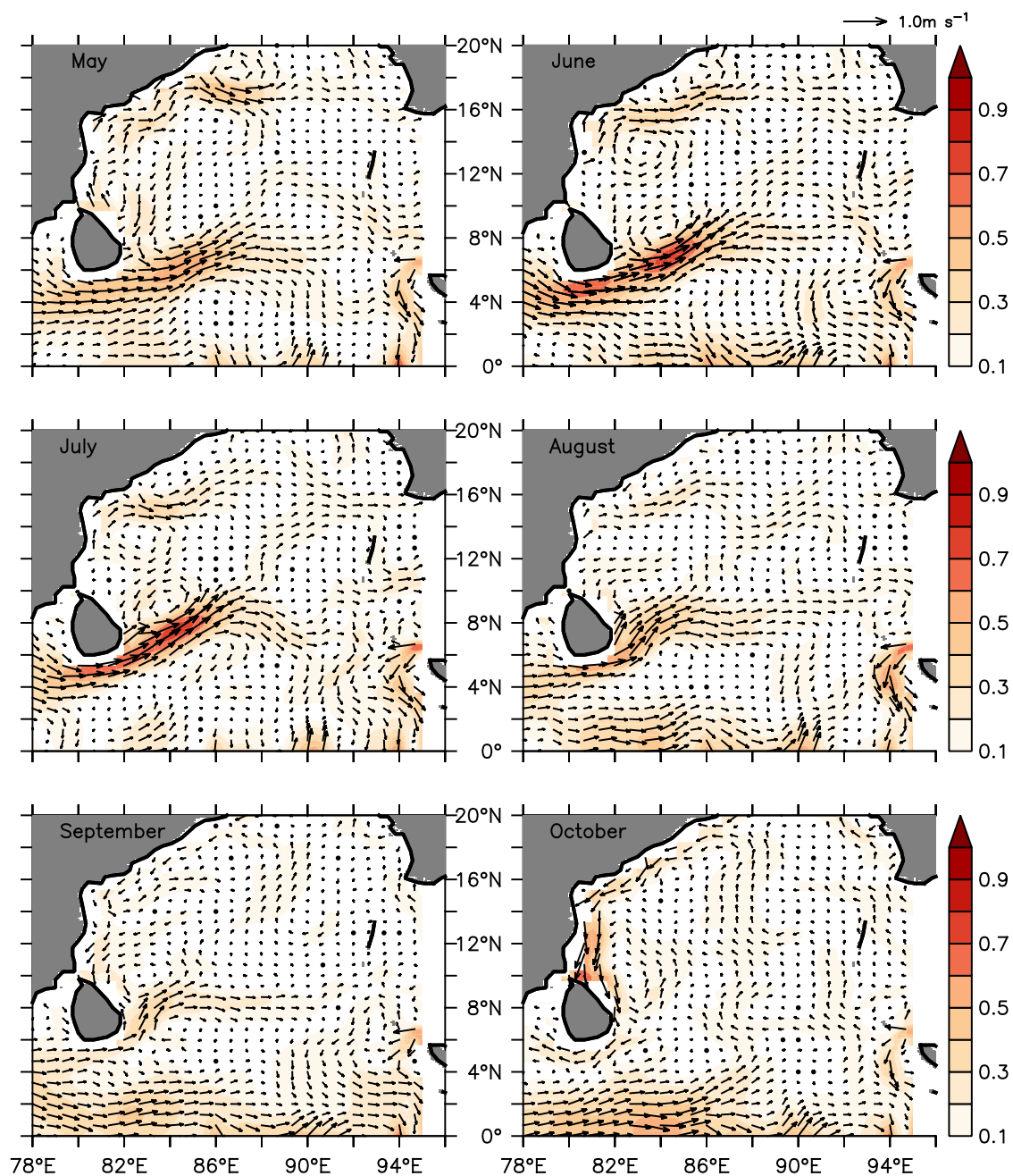


Figure 1: Monthly maps of climatological (2000–2009) currents from OSCAR averaged from May–October. The scale vector (1 m/s) is shown above panel.

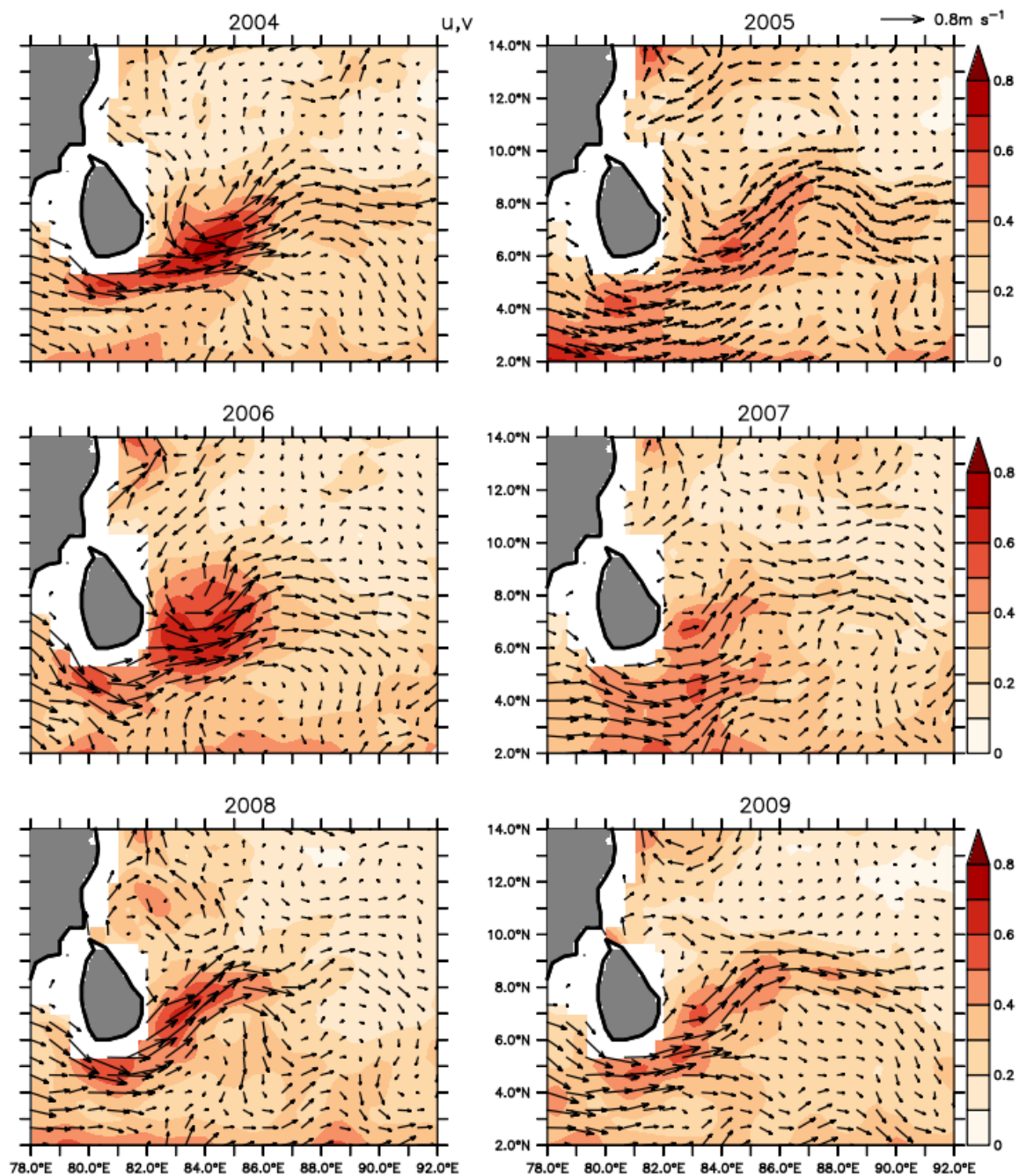


Figure 2: Time mean (June– September) circulation map of SMC from 2004–2009. The scale vector (0.8 m/s) is shown above panel.

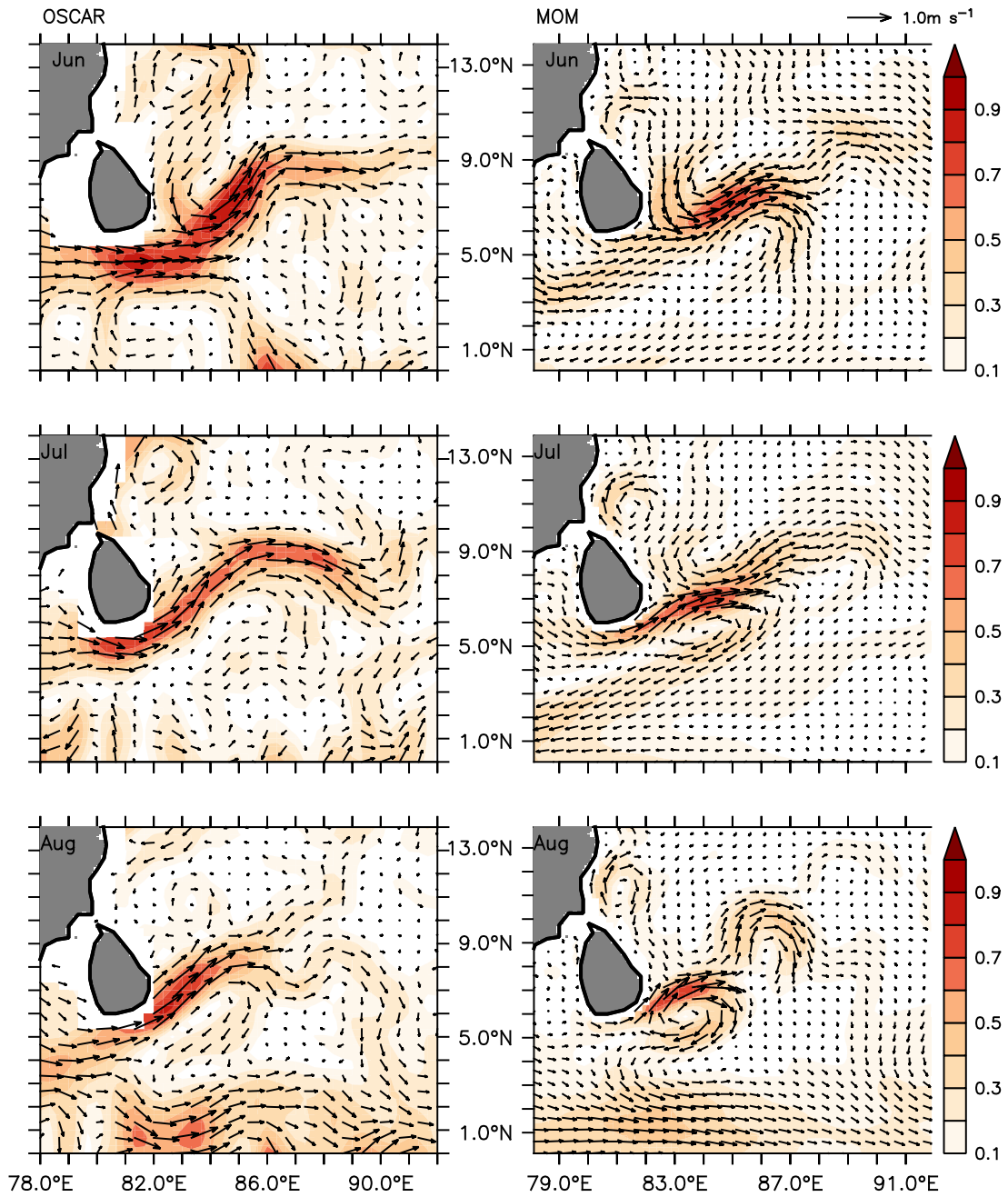


Figure 3: Comparison of monthly maps of currents of southwest monsoon, 2009 from OSCAR (left panels), MOM (right panels). Current vectors overlaid over speed (shading, cm/s). Vectors are of same length in all panels and the scale vector (1m/s) is shown above panel.

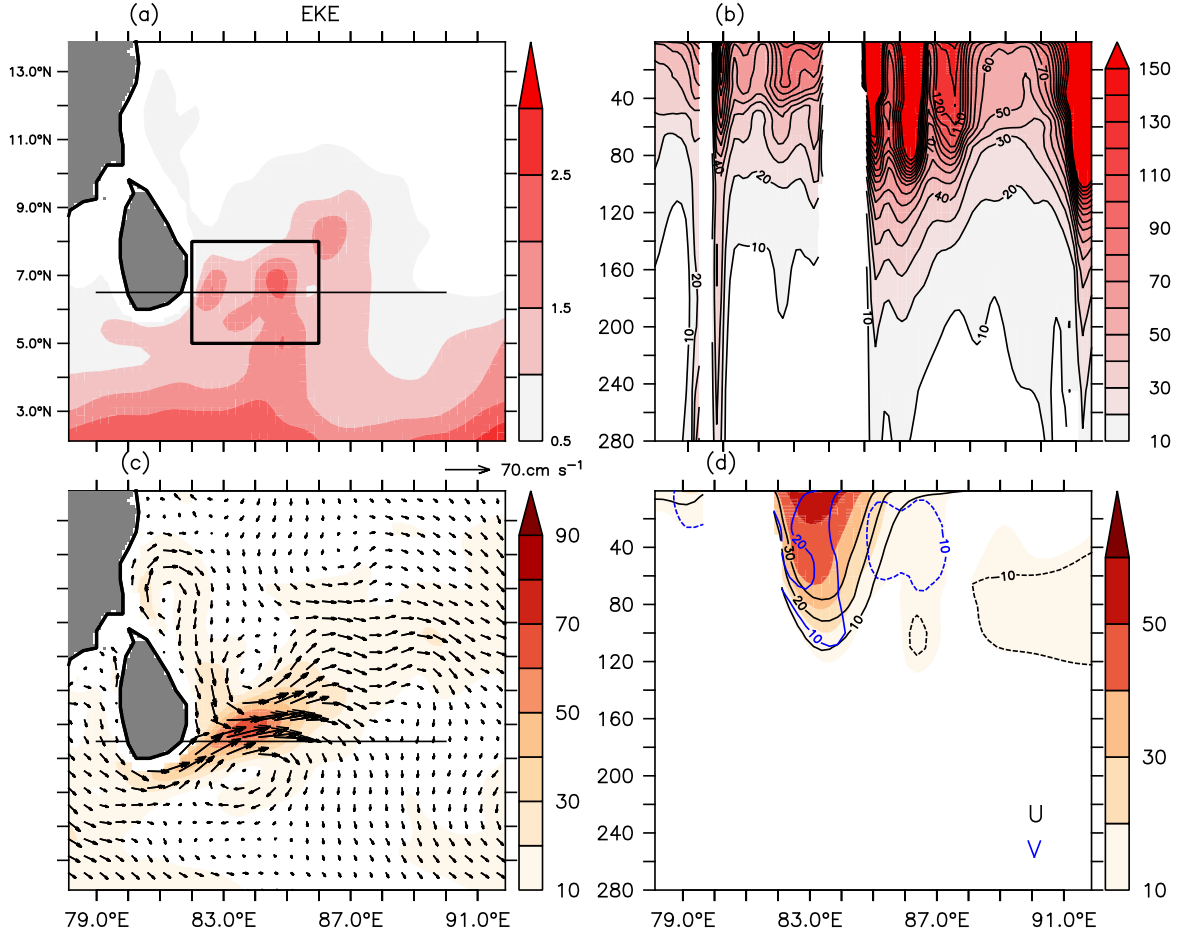


Figure 4: (a) Time mean (June-September) vertically integrated EKE map (cm^3/s^2); (b) depth longitude section along 6.5°N of time mean (Jun-Sep) EKE ($10^{-4} \text{ cm}^2/\text{s}^2$). Vectors are of length 60 cm/s . (c) Time mean (June-September) maps of surface averaged (30m) current vectors from the model overlaid over speed (shading cm/s); (d) time mean depth longitude sections (6.5°N) of zonal velocity (red), meridional velocity (blue) contour spacing of 10cm/s overlaid over speed of current (cm/s).

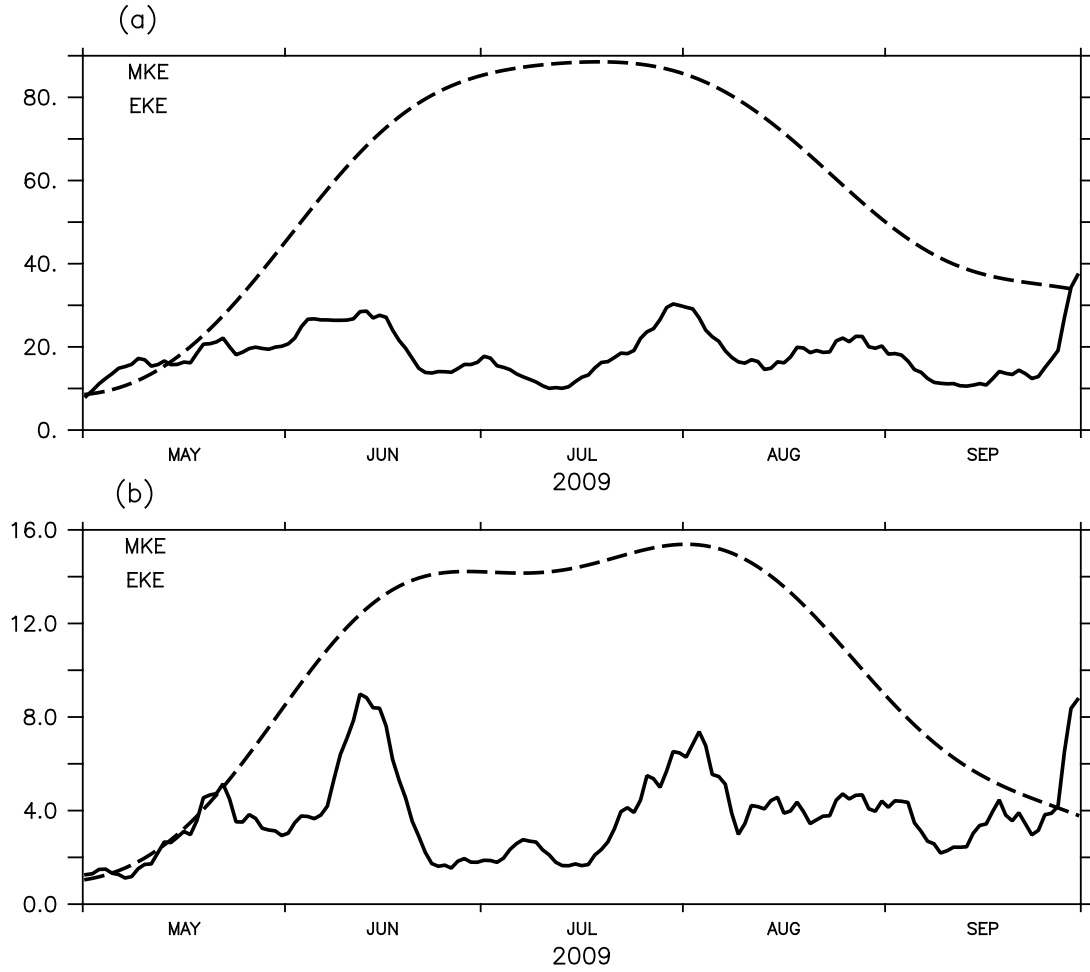


Figure 5: (a) A volume integrated time MKE (dashed lines) and EKE (solid lines) between 82–86°E, 5–8°N, 0–100m. Units– ($10^{16} cm^2/s^2$); (b) volume integrated time MKE and EKE between 84–85°E and 5–7°N.

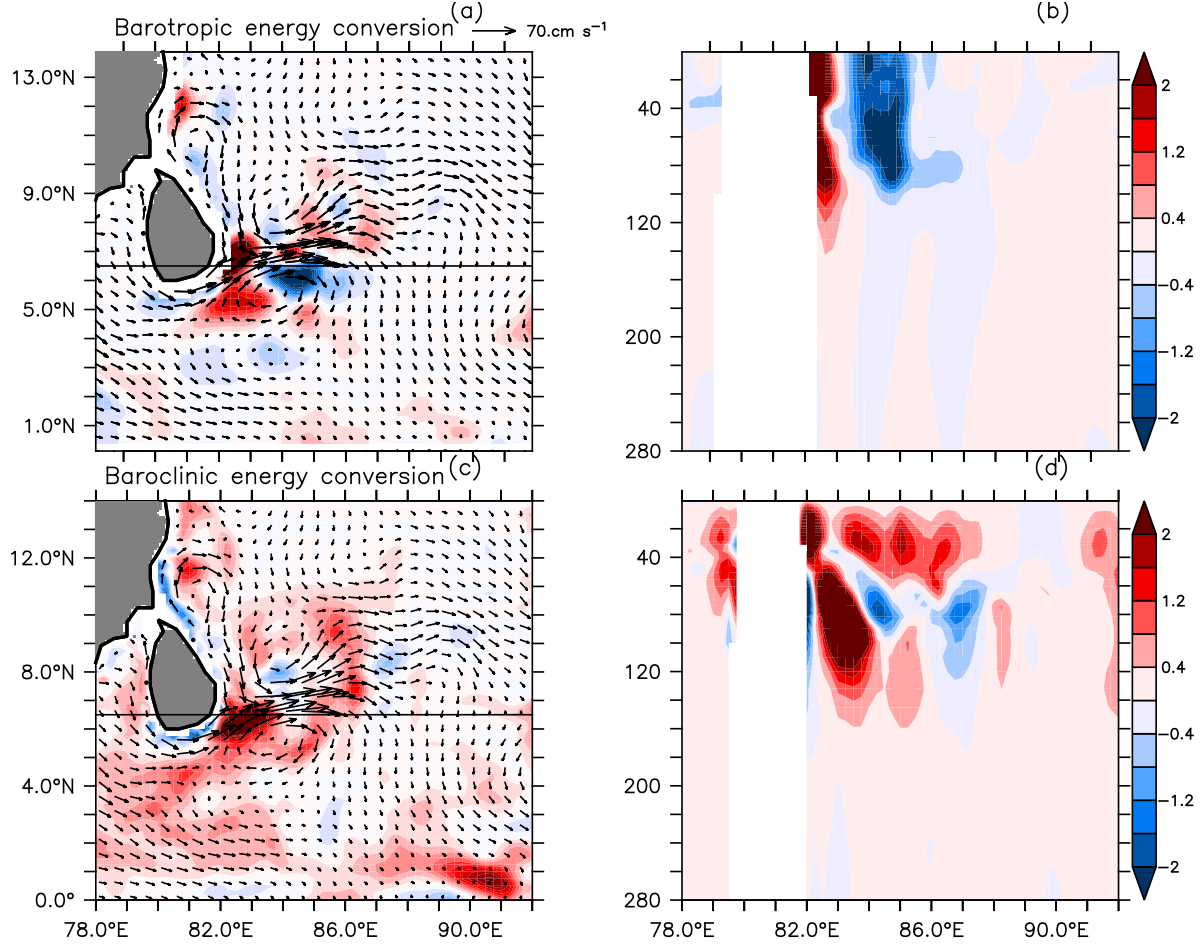


Figure 6: Time mean (June–September) vertically integrated (0–100 m) map of (a) barotropic; (c) baroclinic energy conversion terms (cm^3/s^3). Time mean depth longitude sections ($10^{-4} \text{ cm}^2/\text{s}^3$) of (b) barotropic energy conversion, (d) baroclinic energy conversion at 6.5°N . Time mean current vectors are averaged over 50 m are of same scale (0.6m/s) in both panels.

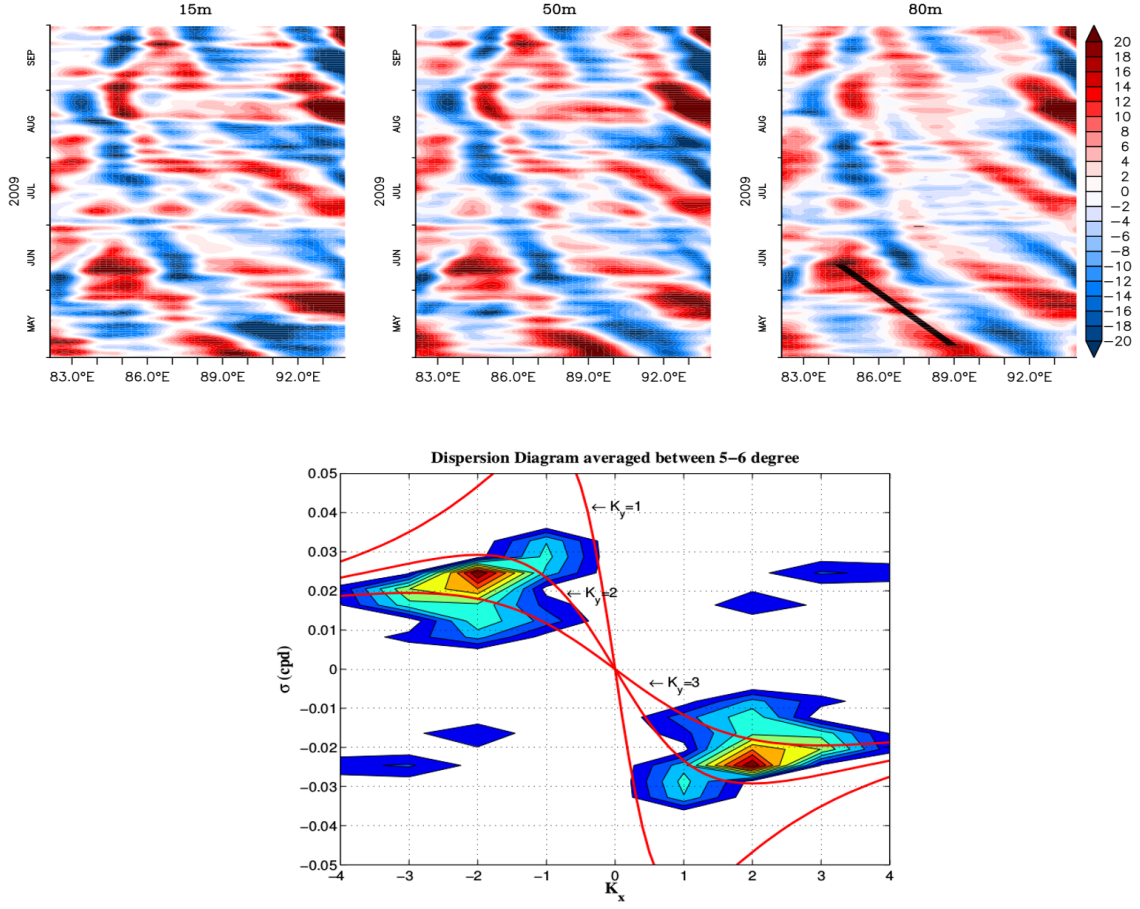


Figure 7: Hovmöller diagram (top) of high passed filtered meridional velocities averaged from 5–6°N. Levels 15 m, 50 m, 80 m. Dispersion diagram (bottom) frequency (σ) versus wavenumber (k).

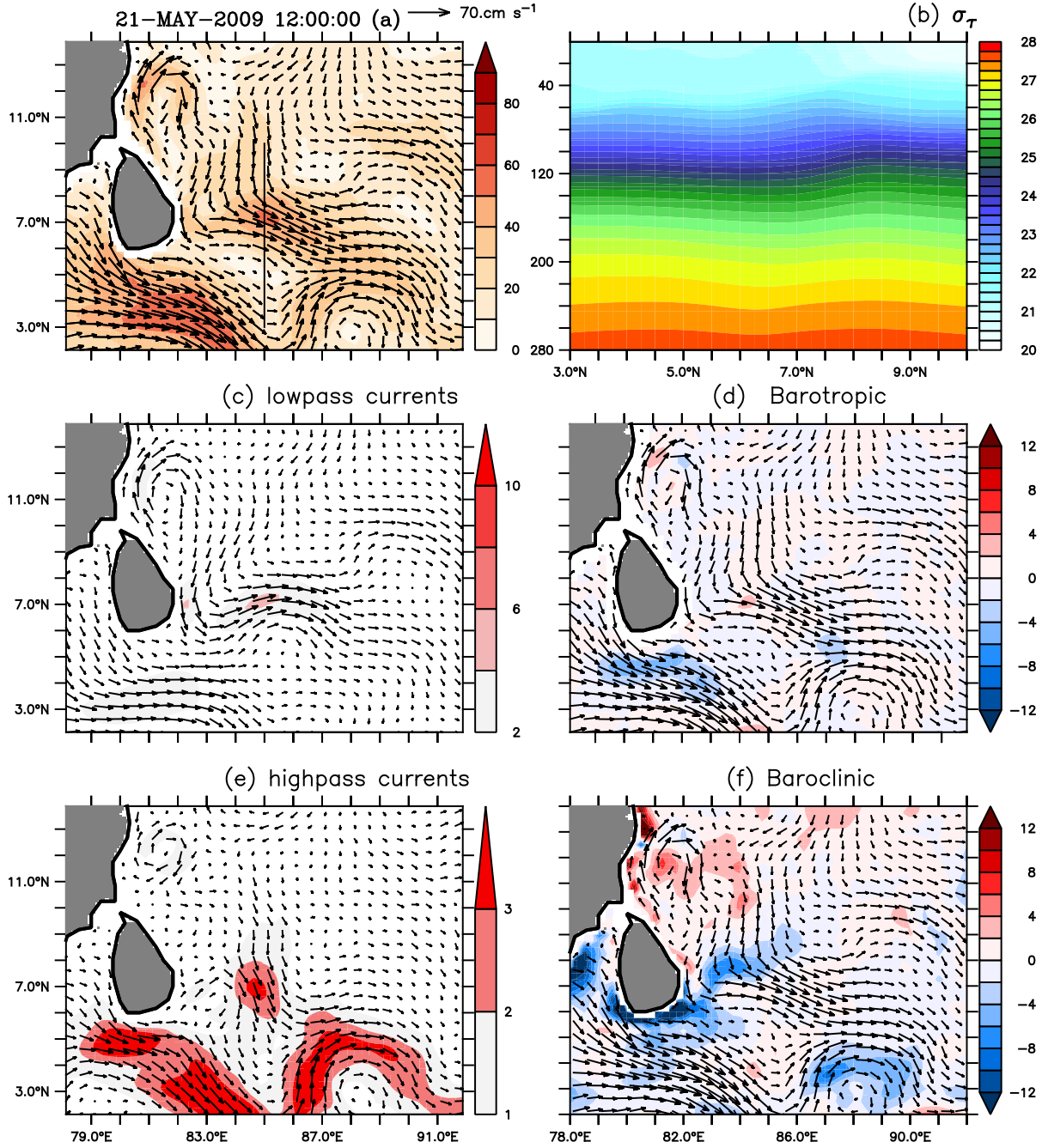


Figure 8: (a) Current vectors overlaid over speed (shading, cm/s) averaged over top 30m; (b) σ_t (kg/m³); (c) 120 day lowpass filtered currents (top 30m depth averaged) as mean flow overlaid over top 100 m vertically integrated map of MKE (shading, cm³/s²); (d) Current vectors (top 30m depth averaged) overlaid over top 100 m vertically integrated map of barotropic energy conversion $-u'_i u'_j \partial \bar{u}_i / \partial y$ (shading, cm³/s³); (e) 120 day highpass filtered currents (cm/s) averaged over top 30 m, as eddies overlaid over top 100 m vertically integrated map of EKE (shading, 10⁶ cm³/s²); (f) Current vectors (top 30m depth averaged) overlaid over top 100 m vertically integrated map of baroclinic energy conversion (shading, cm³/s³). All quantities are 5-day running averaged. Vectors are of same length in all panels and the scale vector is shown in above panel (a).

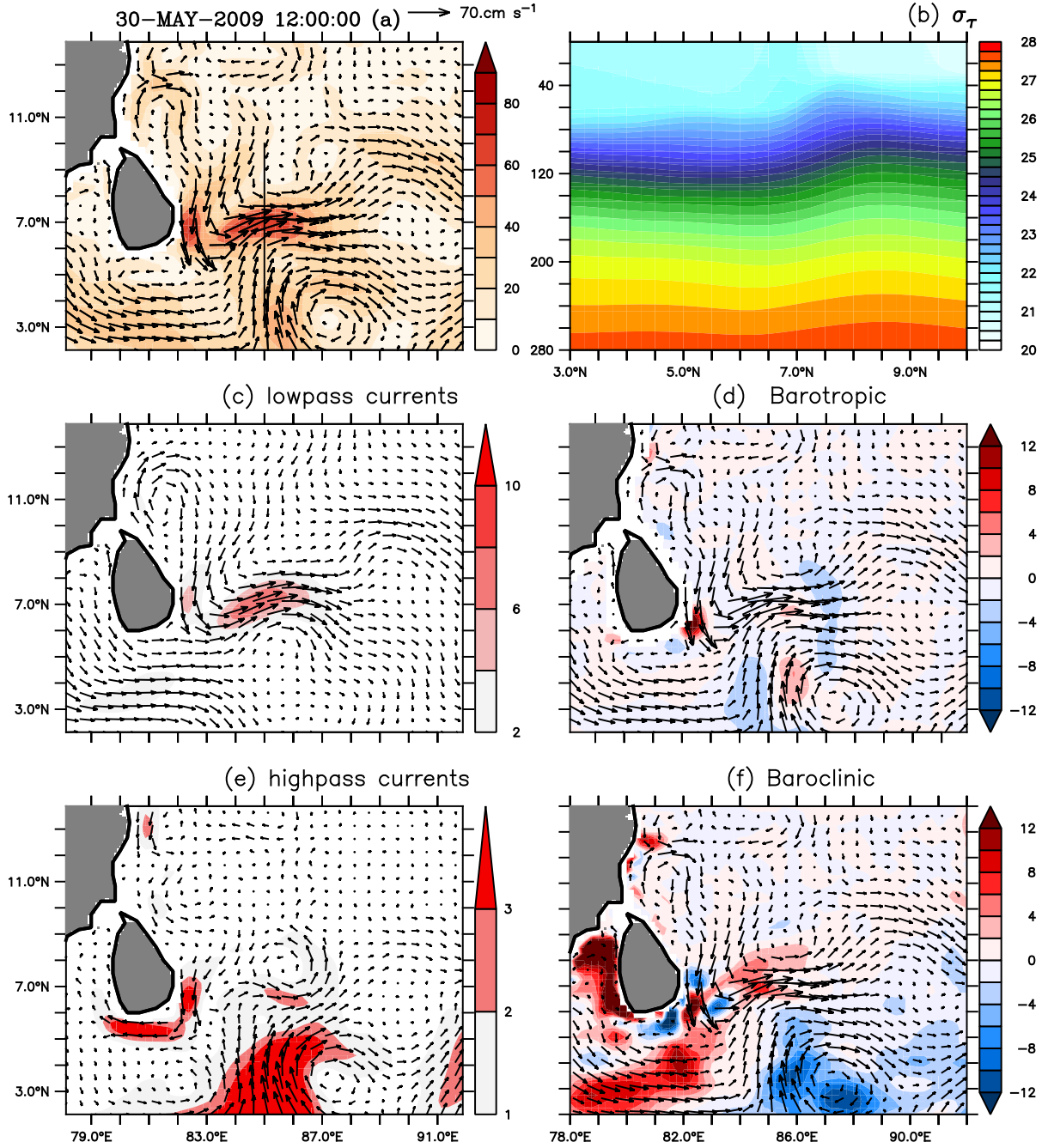


Figure 9: (a) Current vectors overlaid over speed (shading, cm/s) averaged over top 30m; (b) σ_t (kg/m³); (c) 120 day lowpass filtered currents (top 30m depth averaged) as mean flow overlaid over top 100 m vertically integrated map of MKE (shading, cm³/s²); (d) Current vectors (top 30m depth averaged) overlaid over top 100 m vertically integrated map of barotropic energy conversion $-u'_i u'_j \partial \bar{u}_i / \partial y$ (shading, cm³/s³); (e) 120 day highpass filtered currents (cm/s) averaged over top 30 m, as eddies overlaid over top 100 m vertically integrated map of EKE (shading, 10⁶ cm³/s²); (f) Current vectors (top 30m depth averaged) overlaid over top 100 m vertically integrated map of baroclinic energy conversion (shading, cm³/s³). All quantities are 5-day running averaged. Vectors are of same length in all panels and the scale vector is shown in above panel (a).

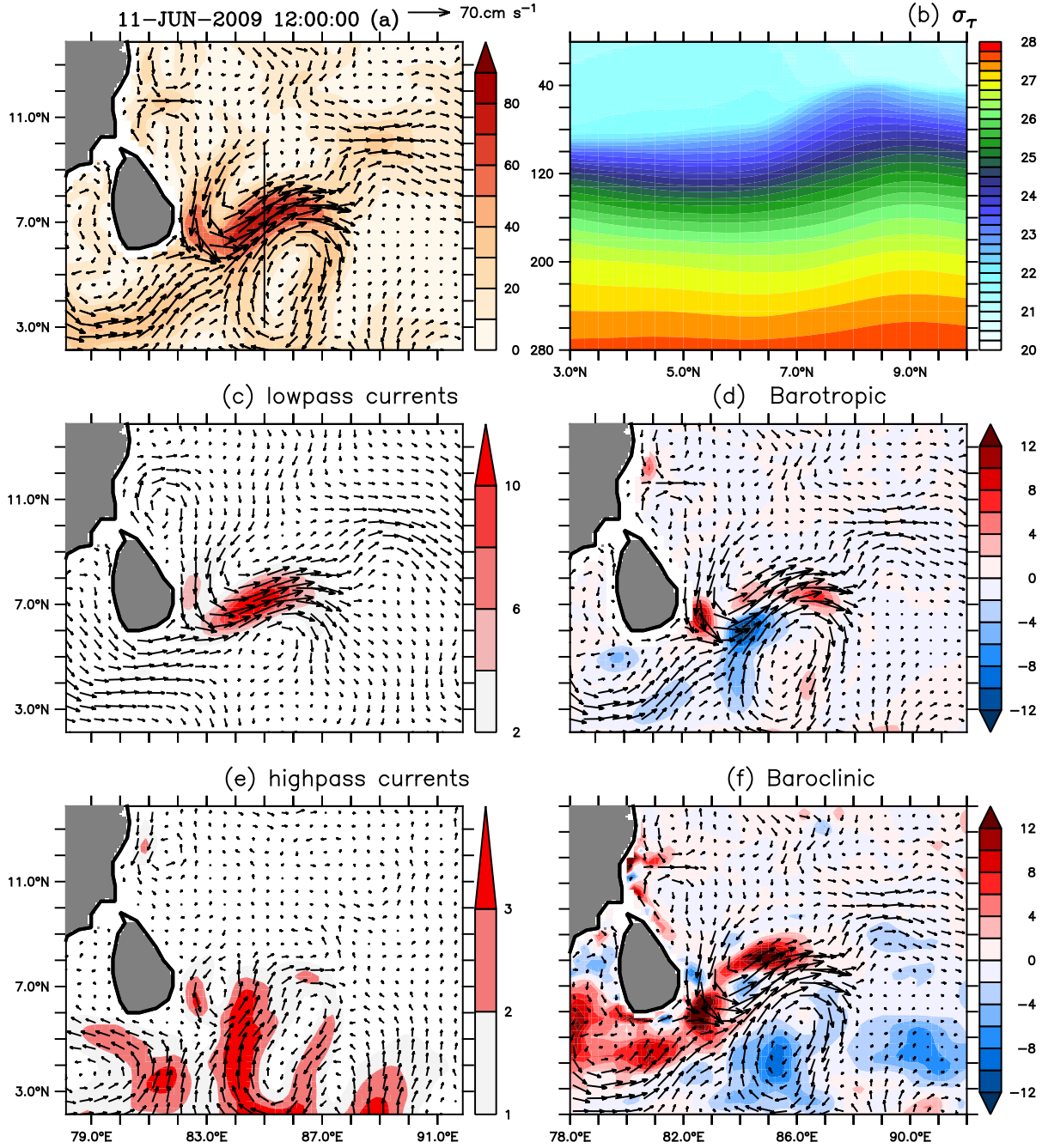


Figure 10: (a) Current vectors overlaid over speed (shading, cm/s) averaged over top 30m; (b) σ_t (kg/m³); (c) 120 day lowpass filtered currents (top 30m depth averaged) as mean flow overlaid over top 100 m vertically integrated map of MKE (shading, cm³/s²); (d) Current vectors (top 30m depth averaged) overlaid over top 100 m vertically integrated map of barotropic energy conversion $-u'_i u'_j \partial \bar{u}_i / \partial y$ (shading, cm³/s³); (e) 120 day highpass filtered currents (cm/s) averaged over top 30 m, as eddies overlaid over top 100 m vertically integrated map of EKE (shading, 10⁶ cm³/s²); (f) Current vectors (top 30m depth averaged) overlaid over top 100 m vertically integrated map of baroclinic energy conversion (shading, cm³/s³). All quantities are 5-day running averaged. Vectors are of same length in all panels and the scale vector is shown in above panel (a).

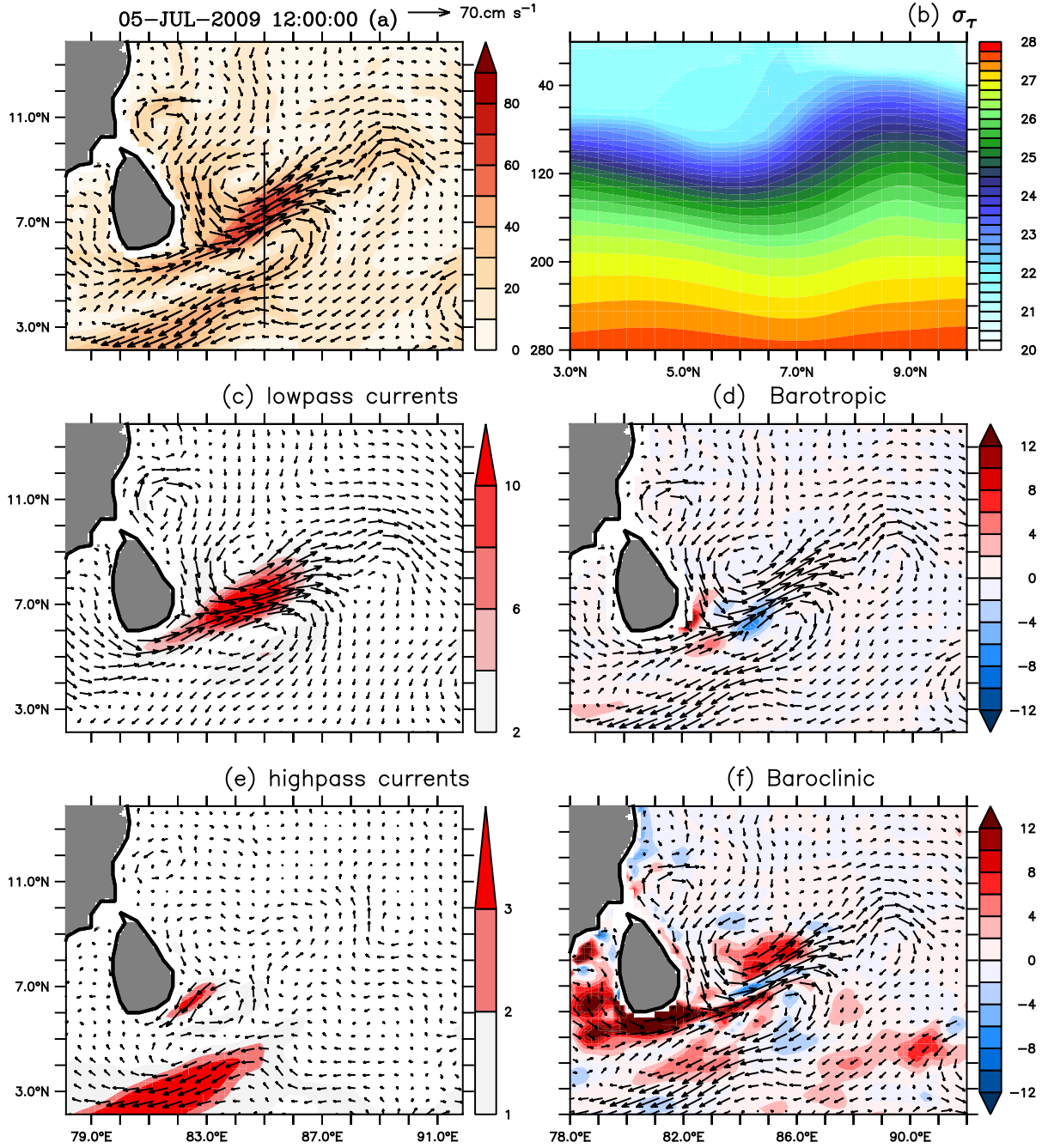


Figure 11: (a) Current vectors overlaid over speed (shading, cm/s) averaged over top 30m; (b) σ_t (kg/m³); (c) 120 day lowpass filtered currents (top 30m depth averaged) as mean flow overlaid over top 100 m vertically integrated map of MKE (shading, cm³/s²); (d) Current vectors (top 30m depth averaged) overlaid over top 100 m vertically integrated map of barotropic energy conversion $-u'_i u'_j \partial \bar{u}_i / \partial y$ (shading, cm³/s³); (e) 120 day highpass filtered currents (cm/s) averaged over top 30 m, as eddies overlaid over top 100 m vertically integrated map of EKE (shading, 10⁶ cm³/s²); (f) Current vectors (top 30m depth averaged) overlaid over top 100 m vertically integrated map of baroclinic energy conversion (shading, cm³/s³). All quantities are 5-day running averaged. Vectors are of same length in all panels and the scale vector is shown in above panel (a).

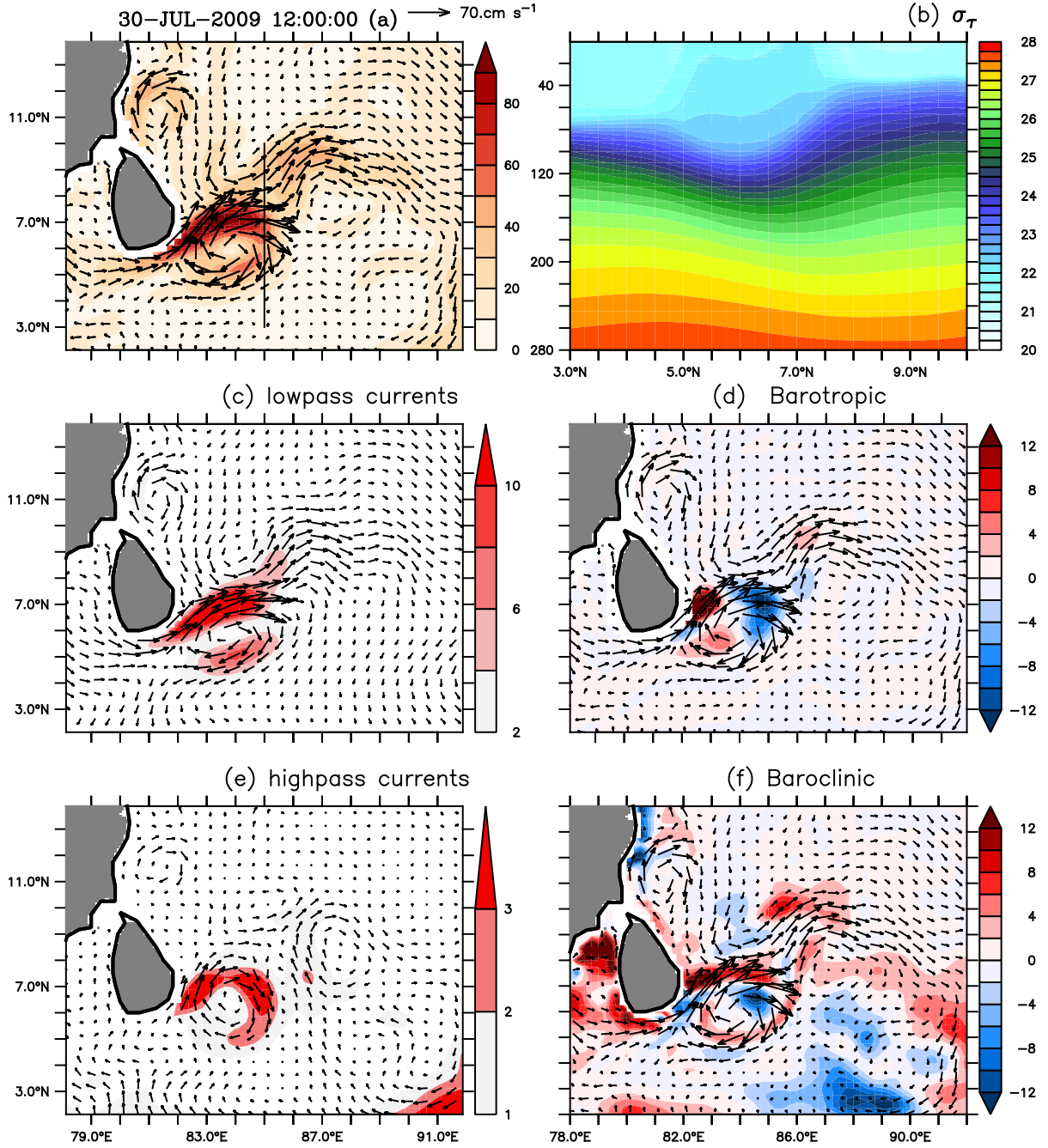


Figure 12: (a) Current vectors overlaid over speed (shading, cm/s) averaged over top 30m; (b) σ_t (kg/m³); (c) 120 day lowpass filtered currents (top 30m depth averaged) as mean flow overlaid over top 100 m vertically integrated map of MKE (shading, cm³/s²); (d) Current vectors (top 30m depth averaged) overlaid over top 100 m vertically integrated map of barotropic energy conversion $-u'_i u'_j \partial \bar{u}_i / \partial y$ (shading, cm³/s³); (e) 120 day highpass filtered currents (cm/s) averaged over top 30 m, as eddies overlaid over top 100 m vertically integrated map of EKE (shading, 10⁶ cm³/s²); (f) Current vectors (top 30m depth averaged) overlaid over top 100 m vertically integrated map of baroclinic energy conversion (shading, cm³/s³). All quantities are 5-day running averaged. Vectors are of same length in all panels and the scale vector is shown in above panel (a).

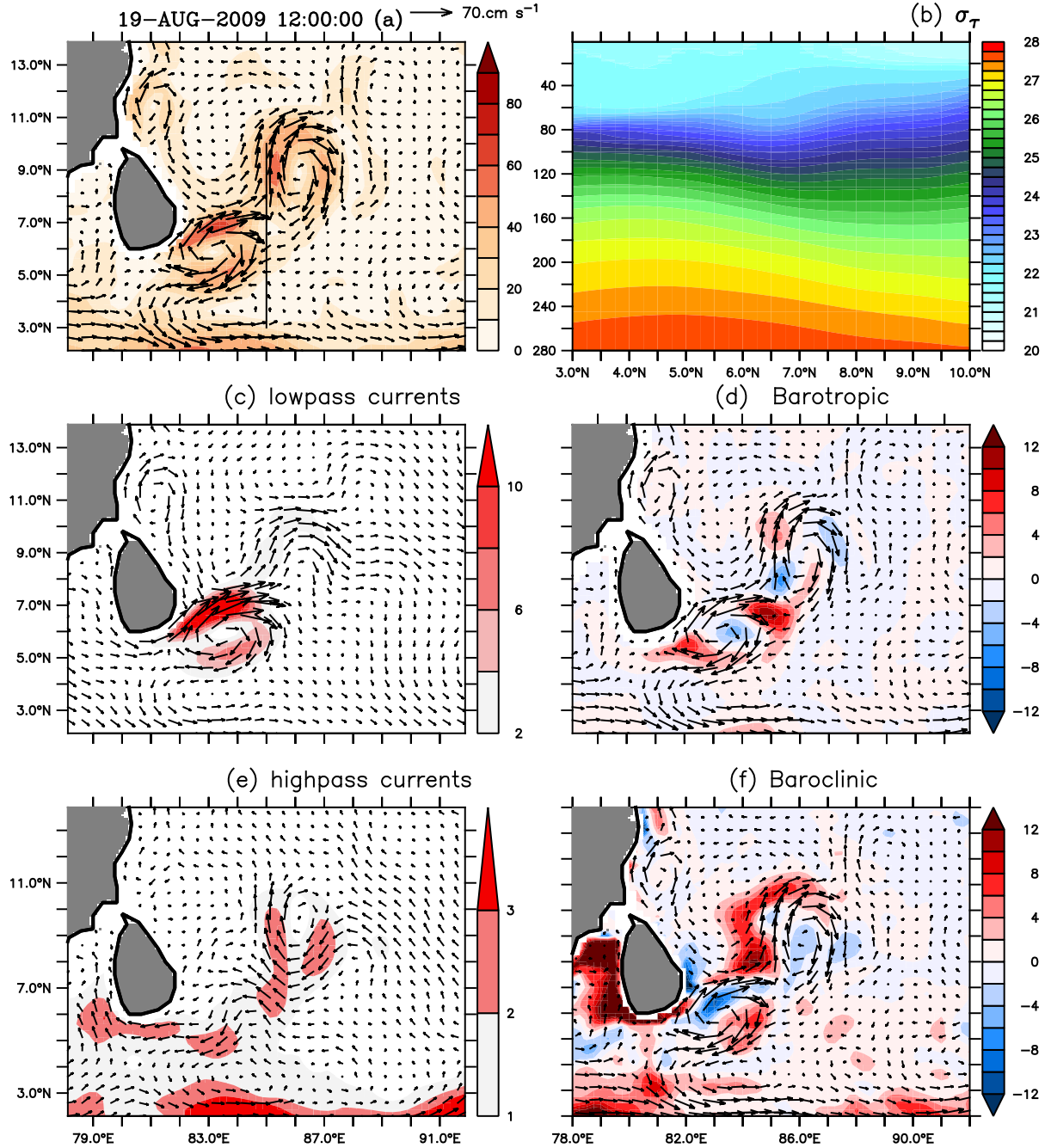


Figure 13: (a) Current vectors overlaid over speed (shading, cm/s) averaged over top 30m; (b) σ_t (kg/m³); (c) 120 day lowpass filtered currents (top 30m depth averaged) as mean flow overlaid over top 100 m vertically integrated map of MKE (shading, cm³/s²); (d) Current vectors (top 30m depth averaged) overlaid over top 100 m vertically integrated map of barotropic energy conversion $-u'_i u'_j \partial \bar{u}_i / \partial y$ (shading, cm³/s³); (e) 120 day highpass filtered currents (cm/s) averaged over top 30 m, as eddies overlaid over top 100 m vertically integrated map of EKE (shading, 10⁶ cm³/s²); (f) Current vectors (top 30m depth averaged) overlaid over top 100 m vertically integrated map of baroclinic energy conversion (shading, cm³/s³). All quantities are 5-day running averaged. Vectors are of same length in all panels and the scale vector is shown in above panel (a).

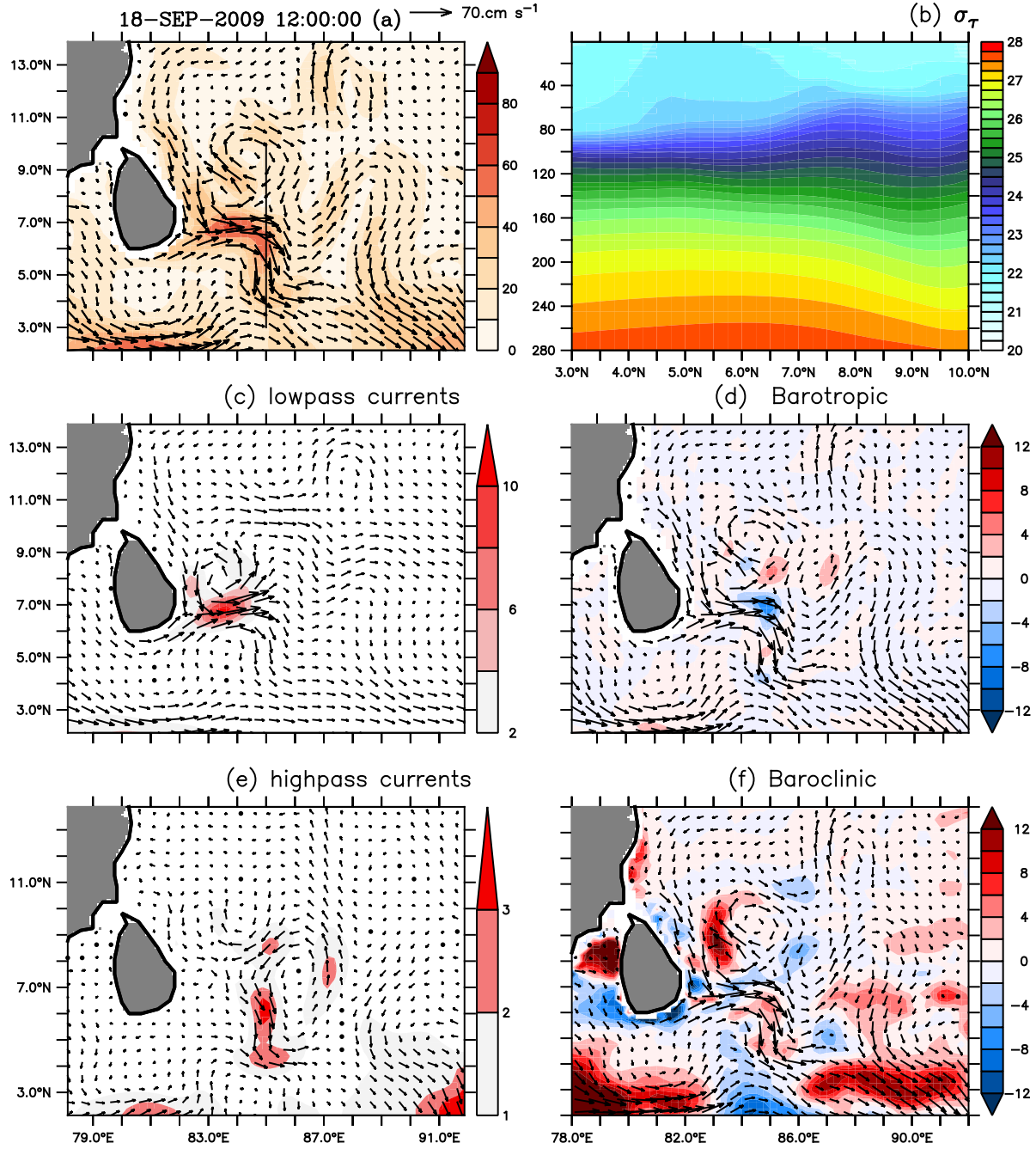


Figure 14: (a) Current vectors overlaid over speed (shading, cm/s) averaged over top 30m; (b) σ_t (kg/m³); (c) 120 day lowpass filtered currents (top 30m depth averaged) as mean flow overlaid over top 100 m vertically integrated map of MKE (shading, cm³/s²); (d) Current vectors (top 30m depth averaged) overlaid over top 100 m vertically integrated map of barotropic energy conversion $-u'_i u'_j \partial \bar{u}_i / \partial y$ (shading, cm³/s³); (e) 120 day highpass filtered currents (cm/s) averaged over top 30 m, as eddies overlaid over top 100 m vertically integrated map of EKE (shading, 10⁶ cm³/s²); (f) Current vectors (top 30m depth averaged) overlaid over top 100 m vertically integrated map of baroclinic energy conversion (shading, cm³/s³). All quantities are 5-day running averaged. Vectors are of same length in all panels and the scale vector is shown in above panel (a).

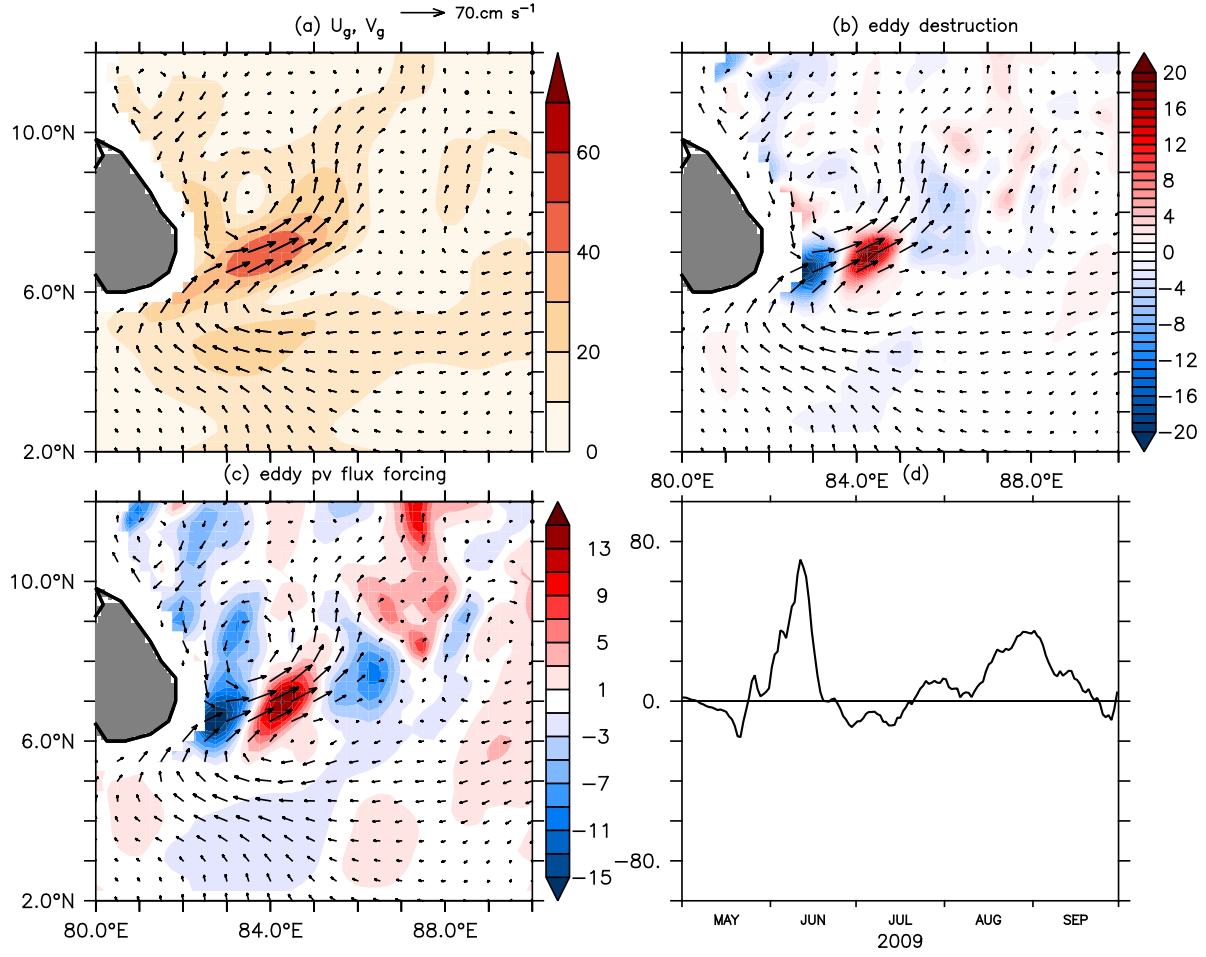


Figure 15: (Clockwise) At 50 m, time averaged (June-September) geostrophic currents vectors overlaid over speeds (shading, cm/s); geostrophic current vectors overlaid over eddy enstrophy destruction term $\mathbf{u}'q' \cdot \nabla \bar{q}$ (shading, 10^{-16} cm/s^2); time series of eddy potential vorticity flux forcing, $v'q'$ (10^{-5} cm/s^2) at 84°E , 6.5°N and at 50 m depth; and eddy pv flux $v'q'$ (shading, 10^{-5} cm/s^2). Vectors are of the same scale as in Panel 1 (top left).

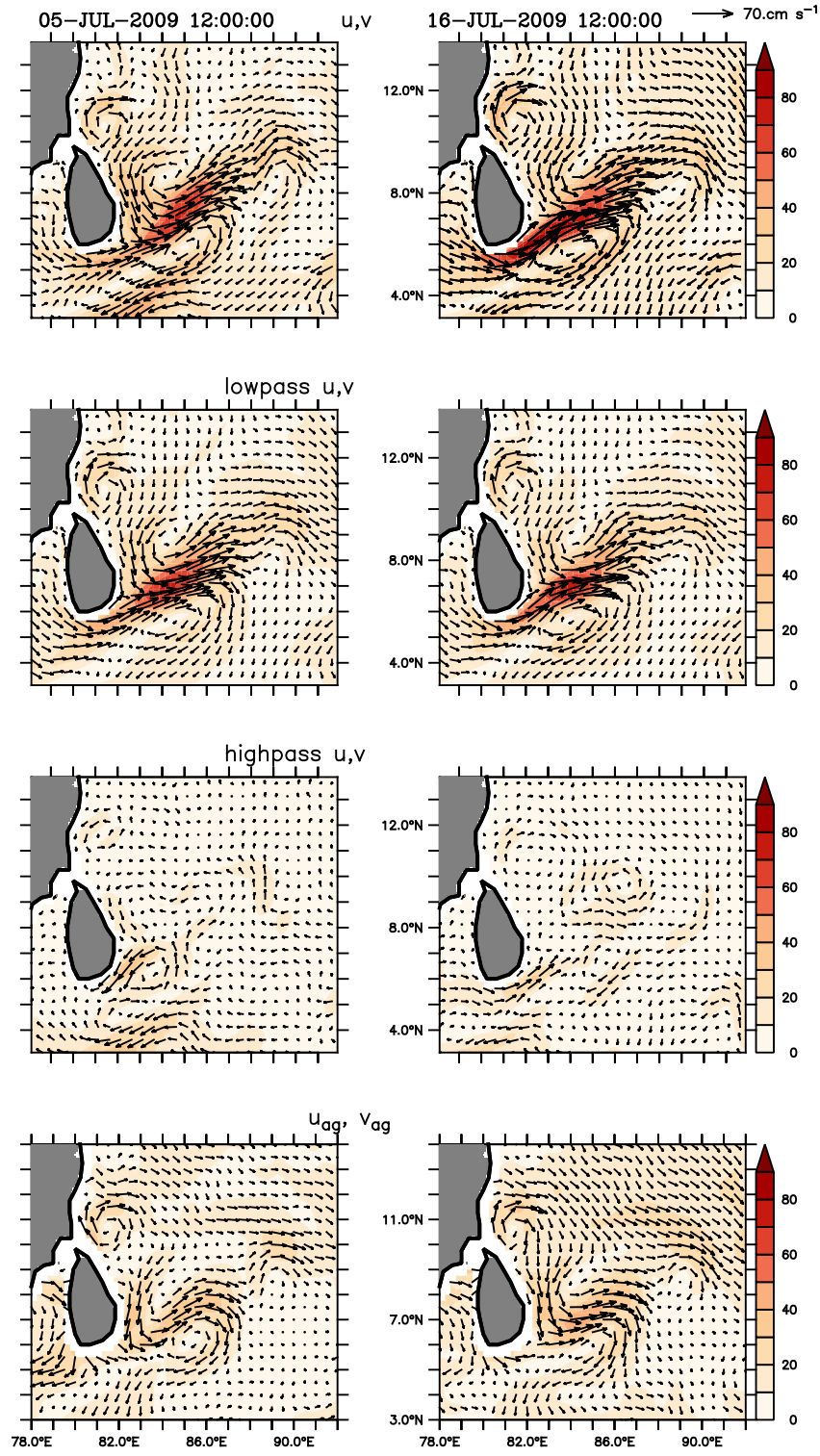


Figure 16: Snapshots of current vectors overlaid over speed (shading, cm/s) averaged over top 30m on 5/07/2009 (left panel) and 16/07/2009 (right panel). First row represents the model currents, second row represents the 120 day low-pass current components, third row shows the 120 day high-pass current components and the fourth row shows the ageostrophic current components. Vectors are of same length in all panels and the scale vector is shown in top panel.

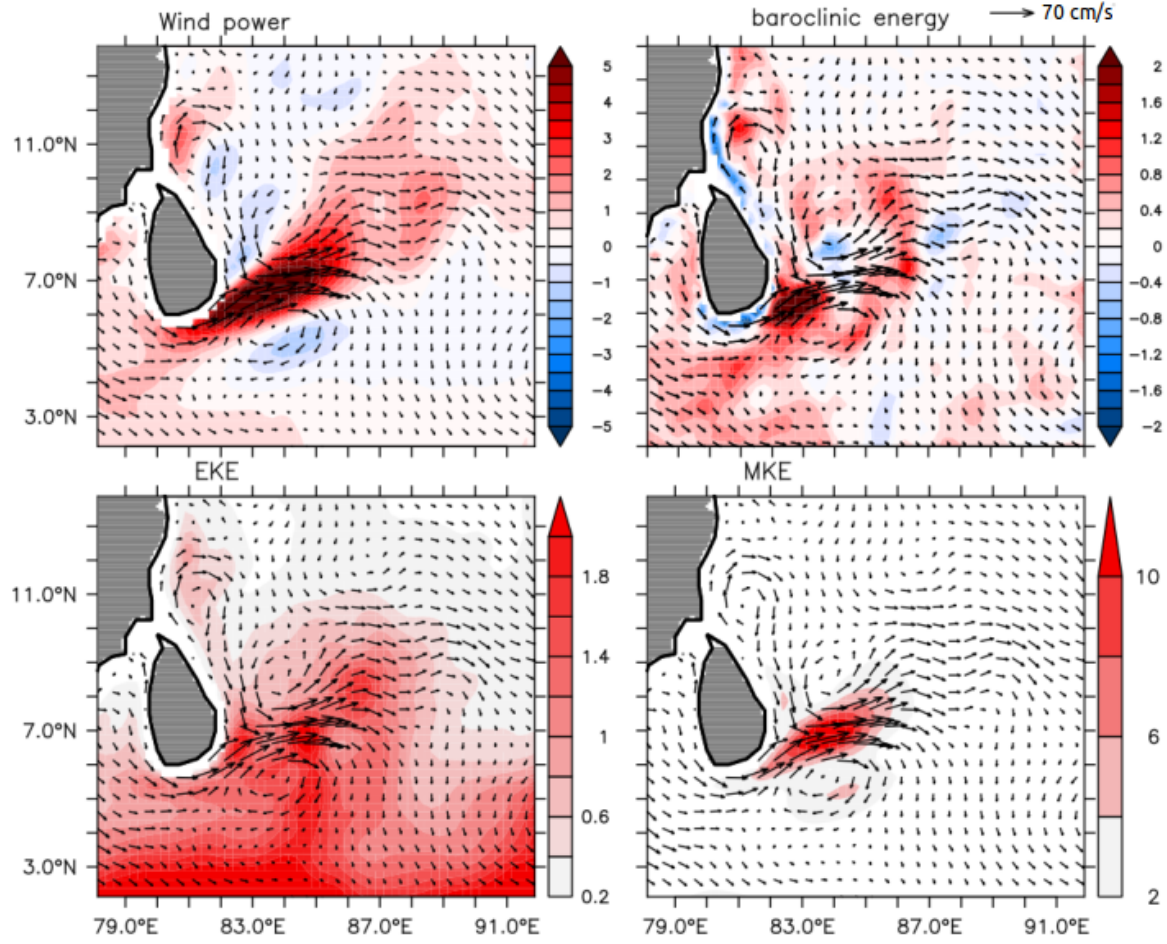


Figure 17: Clockwise: Time mean (June–September) maps of current vectors (averaged over top 30 m) overlaid over wind power (shading, watts); current vectors overlaid over vertically integrated (top 100 m) baroclinic energy conversions (shading, cm^3/s^3) ; current vectors overlaid over vertically integrated (top 100 m) mean kinetic energy and eddy kinetic energy (shading, cm^3/s^2).

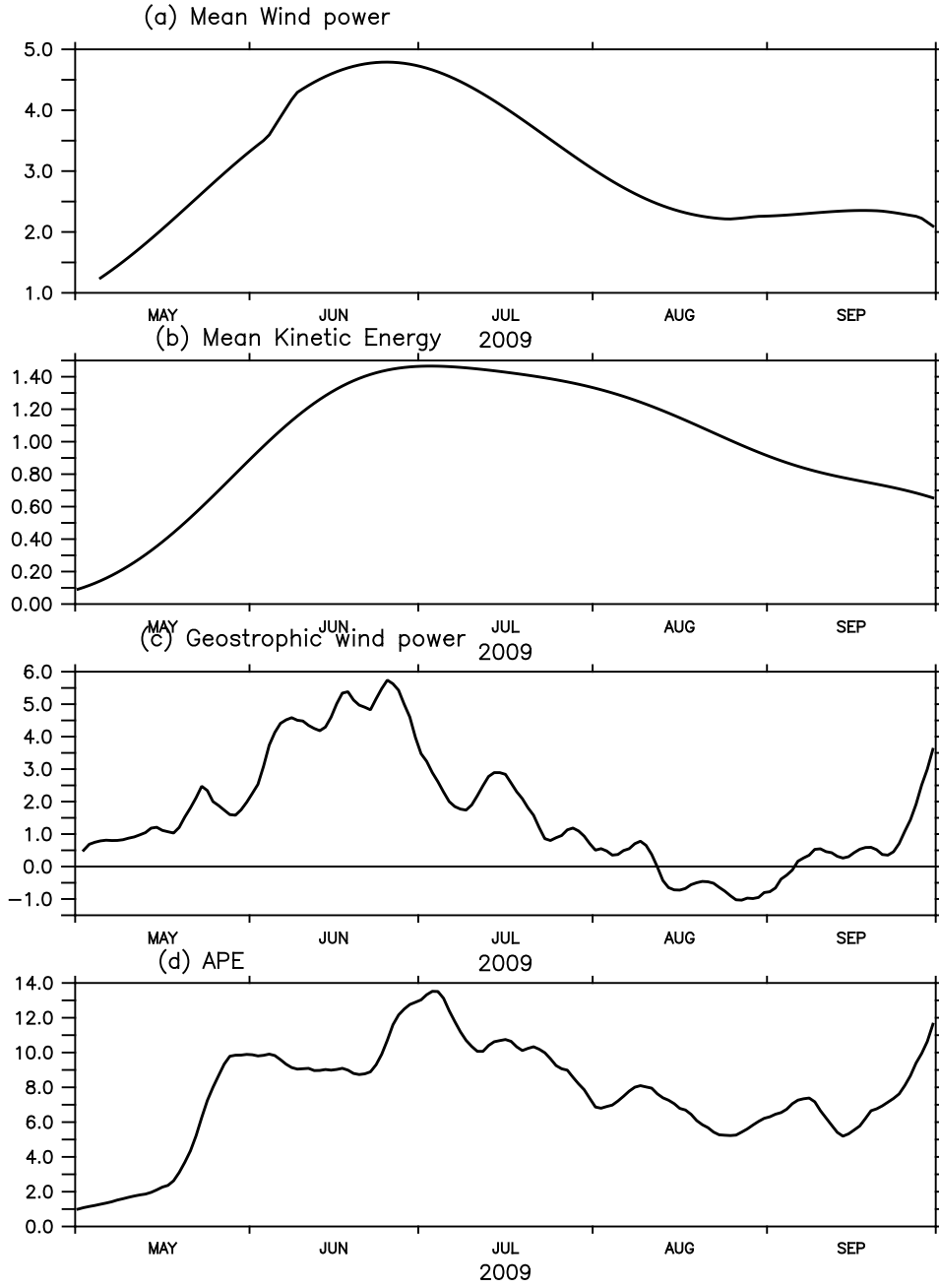


Figure 18: (a) Time series of area integrated ($82-86^{\circ}\text{E}$, $5-8^{\circ}\text{N}$) mean wind Power (5-day smoothened) (top) (10^9 W) (b) surface integrated ($82-86^{\circ}\text{E}$, $5-8^{\circ}\text{N}$) MKE averaged over top 30 m (5-day smoothened) ($10^{14}\text{ Joules/s}^2$); (c) Area integrated ($82-86^{\circ}\text{E}$, $5-8^{\circ}\text{N}$) geostrophic wind power (5-day smoothened) (top) (10^9 W); (d) Volume integrated ($82-86^{\circ}\text{E}$, $5-8^{\circ}\text{N}$, 0–100 m) APE (5-day smoothened) (10^{14} Joules)